



**HAL**  
open science

# On the role of wind and tides in shaping the Gironde River plume (Bay of Biscay)

F. Toubanc, N.K. Ayoub, P. Marsaleix

► **To cite this version:**

F. Toubanc, N.K. Ayoub, P. Marsaleix. On the role of wind and tides in shaping the Gironde River plume (Bay of Biscay). *Continental Shelf Research*, 2023, 253, pp.104891. 10.1016/j.csr.2022.104891 . hal-04292199

**HAL Id: hal-04292199**

**<https://hal.science/hal-04292199>**

Submitted on 18 Nov 2023

**HAL** is a multi-disciplinary open access archive for the deposit and dissemination of scientific research documents, whether they are published or not. The documents may come from teaching and research institutions in France or abroad, or from public or private research centers.

L'archive ouverte pluridisciplinaire **HAL**, est destinée au dépôt et à la diffusion de documents scientifiques de niveau recherche, publiés ou non, émanant des établissements d'enseignement et de recherche français ou étrangers, des laboratoires publics ou privés.



Distributed under a Creative Commons Attribution - NonCommercial - NoDerivatives 4.0 International License



# On the role of wind and tides in shaping the Gironde River plume (Bay of Biscay)

F. Toubanc<sup>\*</sup>, N.K. Ayoub, P. Marsaleix

Université de Toulouse, LEGOS (CNES/CNRS/IRD/UPS), Toulouse, France

## ARTICLE INFO

### Keywords:

Gironde River plume  
Tides  
Wind  
Estuary-Shelf Continuum  
Bulge  
Numerical modelling

## ABSTRACT

We study the Gironde River plume in the Bay of Biscay (North-East Atlantic) using a high resolution modelling approach of the estuary-mouth-shelf continuum. The Gironde River plume flows over a gently sloping shelf where semi-diurnal tides reach an amplitude of 1.3–1.5 m on average; the Gironde River discharge undergoes a significant seasonal variability with floods ( $>1000 \text{ m}^3/\text{s}$ ) in winter and spring. From two years of simulation (2011–12), we document the behavior of the plume under varying forcing conditions. We then discuss the dynamical mechanisms at play, from the estimate of some mechanical energy budget terms and using sensitivity runs: run with no tides, run with filtered atmospheric forcing (no variability at time scales smaller than 30 days) and run with no river runoff. We first show that the plume's properties are determined by the processes occurring in a transition area at the estuary outlet between the Royan and Cordouan sections. The outflow passes through a deep and narrow channel both because of bathymetric constraints and tides. Indeed, tides generate a residual circulation made of anticyclonic and cyclonic vortices with diameters of 5–12 km. Tides also induce intense mixing that strongly modifies the stratification between the two sections. The mean conditions lead to classify the plume as a narrow outflow which is a favorable condition for a bulge to be formed according to the literature. We indeed observe the recurrent formation of a bulge with sharp salinity gradients and a narrow coastal current. The bulge develops in moderate to high discharge conditions, during the spring to neap tides transition and when winds are weak. When the intensity of tides and wind increases, the bulge breaks down and the plume spreads offshore under upwelling wind conditions or along the coast (both in northward and southward directions) under strong eastward wind conditions. Tides are the main driver at the estuary outlet (with a bottom friction term larger by two orders of magnitude than over the adjacent shelf) but winds and atmospheric pressure are the main forcing over the inner shelf. These results evidence the need to model accurately the whole estuary-shelf continuum when studying the fate of riverine waters over the shelf.

## 1. Introduction

River plume dynamics are complex and multiscale, as they integrate the impact of various environmental, physical and atmospheric forcings that do not have the same temporal and/or spatial scales. River discharge can vary significantly in a few hours or days causing major floods, but also be almost constant over long periods of time. Tides have an impact both at the frequency of a few hours (ebb/flood tidal cycle) and several days (neap/spring tidal cycle). Winds can also represent a large range of temporal and spatial scales, from very localized storms to large-scale seasonal winds over the whole shelf. Ambient coastal circulation also plays a major role, with the presence for example of meso-scale eddies interacting with plume waters. These highly variable

forcings are combined with environmental conditions specific to each region: e.g. bathymetry, Coriolis force, estuary mouth width, bottom roughness, etc ... Because of this wide range of scales, numerical modelling is a very powerful tool to study river plumes, to the condition that they allow the representation of their complexity, namely by taking into account the estuary-shelf-deep ocean system as a whole.

The Gironde estuary is located in the Bay of Biscay (Fig. 1) and is one of the largest inputs of freshwater on the French Atlantic coast with the Loire estuary, with similar annual mean discharges of about  $900 \text{ m}^3/\text{s}$  (Puillat et al., 2004), and one of the largest estuaries in Europe. It is fed by the confluence of the Garonne and Dordogne rivers at about 75 km upstream. It is submitted to a macrotidal regime and exposed to strong winds, making it a complex environment to comprehend. The estuary

<sup>\*</sup> Corresponding author.

E-mail address: [florence.toubanc@legos.obs-mip.fr](mailto:florence.toubanc@legos.obs-mip.fr) (F. Toubanc).

mouth is located on a wide shelf (depth <200 m) that follows the French coasts of the Bay of Biscay and extends offshore by ~90 km at 45°N and by ~180 km at 45.75°N. In this area, the water depth increases smoothly in the cross-shore direction; the 100-m isobath is roughly half distance from the coast and the shelf break. Numerous studies have been conducted on the dynamics of the Gironde estuary. The first studies were motivated by the need to understand the dynamics of the sediments and turbidity maximum in the estuary (for example Allen et al., 1980; Sottolichio et al., 2001). They showed that sediment dynamics are mainly tidally driven, with a strong impact of tidal asymmetry. Stratification in the estuary can change from well-mixed to partially-mixed depending on tidal and fluvial regimes. Tidal dynamics and tides impact on

morphodynamics or water quality are still the subject of much research (for instance Etcheber et al., 2011; Ross et al., 2019).

The fate of the Gironde waters over the shelf has been studied both with observational and numerical modelling studies (Lazure and Jégou, 1998; Froidefond et al., 1998; Hermida et al., 1998; Puillat et al., 2004; Costoya et al., 2017; Ayouche et al., 2021). According to the observations of Castaing (1984) and the numerical simulations of Lazure and Jégou (1998), the Gironde plume spreads northward and alongshore during winter, while the shelf stratification is weak. During spring, changes in the river discharge and the dominant winds may induce a shift in the path of the plume that can spread more southward or offshore (Lazure and Jégou, 1998; Puillat et al., 2004). Estuarine waters

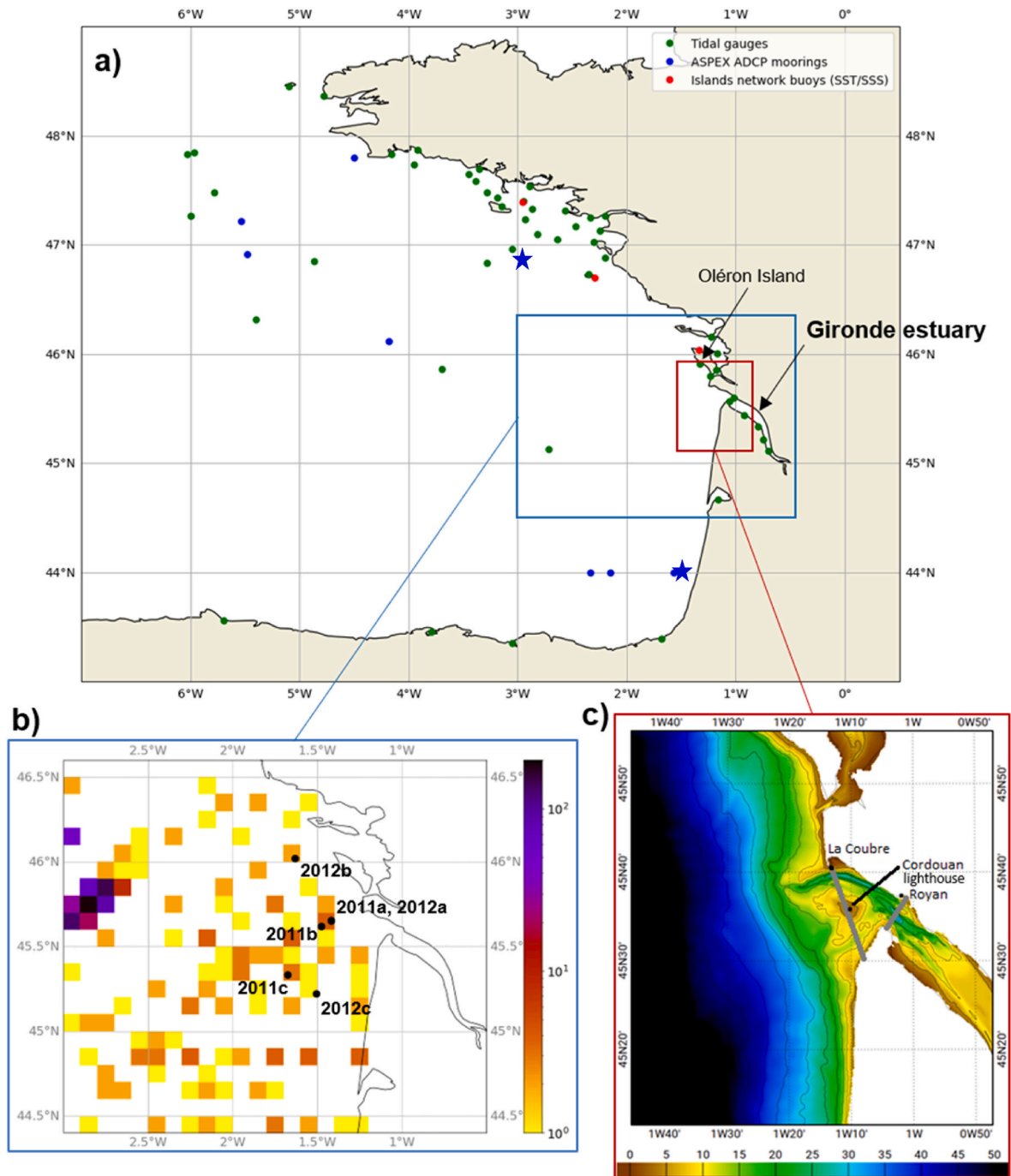


Fig. 1. a) Location of the main in situ data points used for model assessment, b) Spatial distribution of CORA-IBI database profiles used for model validation. Colorbar: number of profiles ( $0.1^\circ \times 0.1^\circ$  grid). Black dots: example profiles detailed in Fig. 2. Blue stars: example ASPEX moorings detailed in Fig. 3, c) Bathymetry of the Gironde outlet and adjacent shelf area in the BOBSHELF configuration (m).

are then mixed with seawater. Lazure and Jégou (1998) find that in winter, winds have the same orientation as the density-driven currents, enhancing the northward propagation of the plume. In spring, winds are often in the opposite direction, favoring offshore and southward spreading. Lazure and Jégou (1998) did not provide results for the summer and autumn seasons, as they are often low discharge periods. Costoya et al. (2017) based their study on MODIS turbidity data and showed that downwelling winds favor the retention of the plume near the coast, while upwelling winds favor its extension and dilution with shelf waters. From AVHRR/NOAA satellite images, Hermida et al. (1998) mention that the plume has spread southward in July 1993 after several days of northwesterly winds. Using in situ data and a Lagrangian model based on altimetry-derived geostrophic currents, Reverdin et al. (2013) evidence freshwater spreading from the Aquitaine shelf in April 2009 to the deep ocean by July. They underline the impact that such freshwater exports may have on larva transport from species initially found off the Gironde estuary.

As shown in the literature, the fate of the Gironde waters from the estuary to the deep ocean results from a complex sequence of transport and dilution processes. Given their impact on the hydrology over the shelves and possibly further in the deep ocean and their influence on water quality and ecosystems, these processes deserve to be better understood. In this paper we propose to complement the previous studies, focusing in the near and mid field, at the junction between the estuary and the Aquitaine shelf, where the dynamics have not been studied in details so far. Our objective is to provide answers to the following questions: what are the main pathways of the estuarine waters there? What is the influence of tides and of the wind variability?

To address this issue, we use numerical simulations where the estuary-shelf-deep ocean continuum is represented with a size varying mesh and a refinement of the grid near the mouth. The estuary itself is modelled up to the confluence of the Garonne and Dordogne rivers, which is in the vicinity of the saline intrusion limit. Indeed, the plume dynamics is intrinsically driven by the water mass transformation that occurs inside the estuary. The configuration includes realistic tidal, atmospheric and large-scale circulation forcings. The modelled plume displays a large variety of patterns and is subject to a strong variability at hourly time-scales. We identify patterns that last for several days and are observed at least twice over the study period (two years).

The main recurrent pattern is a bulge, that is an anticyclonic closed circulation; bulges have been recognized as typical plume structures in the literature from theoretical or modelling studies and in a few observations (for a review, see for instance Horner-Devine et al., 2015). To our knowledge, the case of the bulge in the Gironde has only been identified and studied by Ayouche et al. (2021). These authors simulate two contrasted 30-day periods (March and August), from a high-resolution configuration of the whole Bay of Biscay, where the estuary bathymetry is however not fully represented. They analyze the nonlinear processes leading to instabilities and frontal dynamics responsible for mixing. In this paper, we propose a complementary study by analyzing several bulge occurrences in an attempt to identify the conditions for the formation and destabilization.

More extensive plumes also occur in our 2-year simulation. We identify in particular two cases of both spreading of the plume to the west/northwest and to the south and north along the coast. As shown in the literature, these events can be linked to different directions of the wind. We also show that floods can impact the circulation at the estuary mouth and influence the path of estuarine waters. The explicit representation of this area in our configuration allows us to highlight the changes in circulation occurring there. Besides, to further investigate the role of tides, river discharge and wind variability, we conduct sensitivity experiments.

The rest of the paper is organized as follows: the model configuration and data used are detailed in Section 2. Section 3 presents the model assessment. In Section 4, we show the forcings at play in our 2-year simulation and discuss the main patterns of the plume over a 2-year

mean and its sensitivity to the forcings. In Section 5, we discuss in details the recurrent occurrence of a bulge throughout the simulation and we identify the conditions for its formation and its relaxation. We also explore the cases of larger plumes with a west/north-west or north/south extension. We conclude the paper by recalling the main findings of this study and discussing potential perspectives.

## 2. Model configuration, data and methods

### 2.1. SYMPHONIE model and BOBSHELF configuration

The BOBSHELF configuration and SYMPHONIE code were previously described in Toubanc et al. (2018). SYMPHONIE is a primitive equations model, developed for regional and coastal studies (Marsaleix et al., 2006, 2008), and based, in this configuration, on Boussinesq and hydrostatic assumptions. The k-epsilon turbulence closure scheme is implemented as described in (Michaud et al., 2012). The horizontal curvilinear has a resolution varying from 2.7 km at the western open boundary to less than 300 m in the most resolved areas, including the Gironde estuary (see Toubanc et al., 2018, their Fig. 2). On the shelf, at the Gironde outlet, the horizontal resolution ranges between 250 m at the coast and 700 m at the 100 m isobath approximately. The bathymetry has been locally updated over the shelf and in the Gironde estuary. Intertidal areas are resolved with a wetting and drying scheme. One of the main evolutions in the BOBSHELF configuration resides in the use of VQS (vanishing quasi-sigma) coordinates instead of sigma coordinates in SYMPHONIE, as in Estournel et al. (2021). The VQS coordinate is generally used to avoid an excess of vertical levels in very shallow areas while maintaining an accurate description of the bathymetry and reducing the truncation errors associated with the sigma coordinate (Siddorn and Furner, 2013; Dukhovskoy et al., 2009). In BOBSHELF, the number of vertical levels ranges from 55 in the deep ocean to 5 in the shallowest areas. In the Gironde estuary and adjacent inner shelf, all the levels have the same thickness: from ~2 m over the shelf to less than 1 m in the shallowest areas.

Atmospheric forcing is provided by the ECMWF operational analyses (3-h fields, 1/8° resolution). Tidal forcing with 9 constituents (M2, S2, N2, K2, O1, P1, K1, Q1, M4) is prescribed by a tailored tidal simulation performed with the T-UGOm tidal model, with the same horizontal grid and bathymetry as the ones used in SYMPHONIE. This method for tidal forcing was detailed and validated in Toubanc et al. (2018). The 3D non-tidal circulation is prescribed at the open boundaries from the CMEMS IBI Reanalysis Daily Physical product, a 1/12° resolution reanalysis over the North East Atlantic, with data assimilation. The IBIRYS forcing consists of daily fields of temperature, salinity, horizontal current velocities and sea surface elevation.

Daily river discharges are prescribed for 6 rivers (Adour, Garonne and Dordogne, Charente, Loire and Vilaine). The data are obtained from the French national service 'Banque Hydro'. The model grid covers the estuary from the mouth to the confluence of the Garonne and Dordogne rivers. However, tides influence the rivers farther, over ~90 km upstream of the confluence. In order to model the damping of the tides in the rivers, both tidal rivers are simulated by channels, in a 2DV representation (that is with just one cell in the transverse direction) as done for instance by MacCreedy et al. (2009) in the Columbia River or by Piton et al. (2021) and Nguyen-Duy et al. (2021) in the Red River delta with the Symphonie model. The Dordogne and Garonne discharges are then prescribed at the most upstream point of the channels (see Nguyen-Duy et al., 2021; their appendix B in supplementary material).

### 2.2. Data for model assessment

Tides play a major role in the Bay of Biscay and Gironde estuary dynamics. They are then extensively validated, using a total of 52 tidal gauges for comparison of the amplitudes and phases of the main tidal constituents. Tidal harmonics calculated from satellite altimetry data

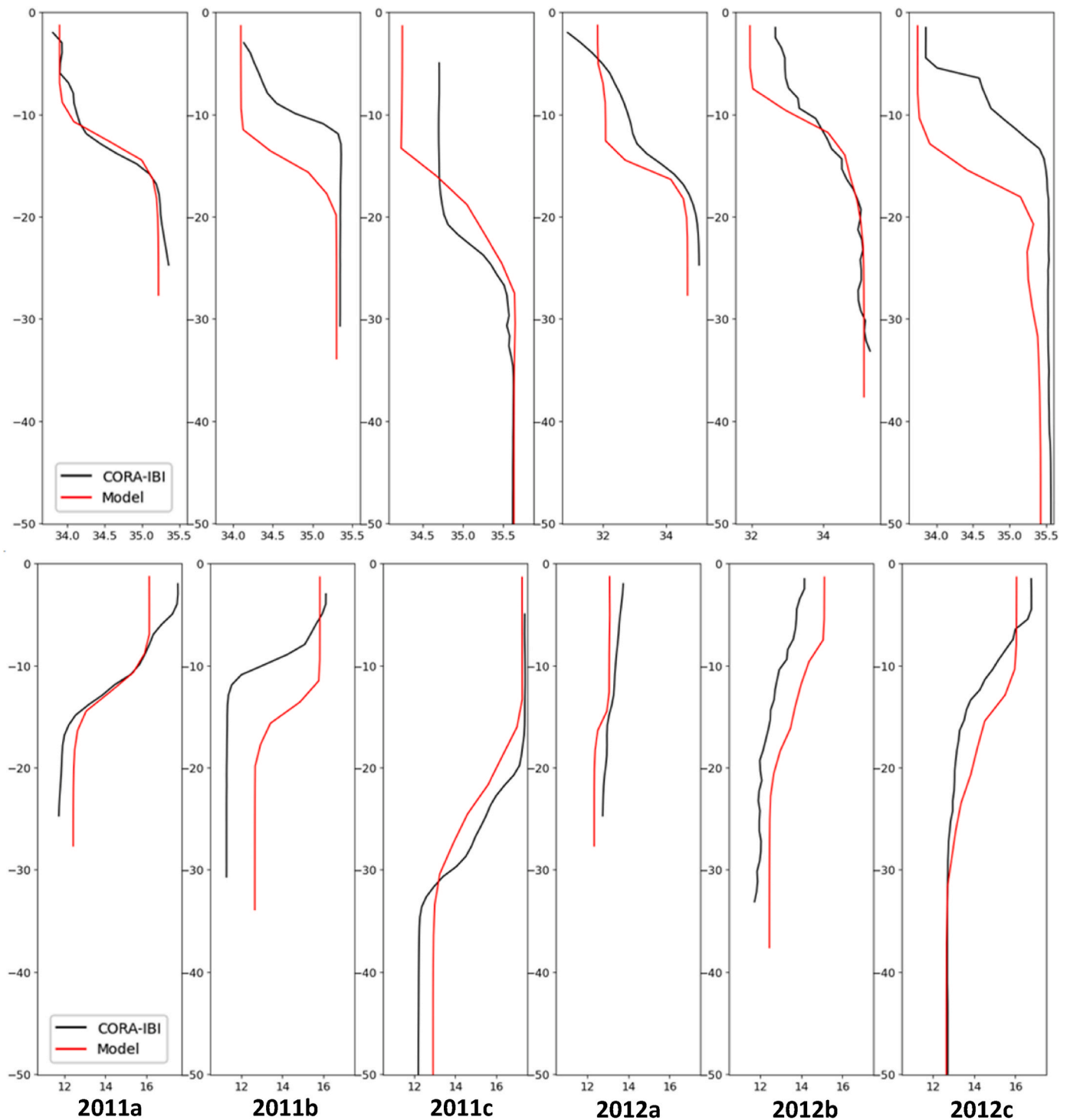


Fig. 2. Salinity (top panel) and temperature profiles (bottom panel) comparison between the REF simulation (red) and the CORA-IBI data (black).

are also used. Along-track amplitudes and phases are estimated from the sea surface height measurements of several satellites (TOPEX/Poseidon, Jason 1, Jason 2), through harmonic analysis (Lyard et al., 2021).

We also compare model outputs with temperature and salinity data. We use the CORA-IBI database (temperature and salinity profiles) compiled by IFREMER (Szekely et al., 2017), as well as in situ observations from the IMR network (IFREMER). A gridded ( $1^\circ \times 1^\circ$ ) database giving monthly estimates of the SSS (sea surface salinity) in the Atlantic Ocean (Reverdin et al., 2007; Alory et al., 2015) is also used.

Currents are compared to 2D daily averages of cross-shore and along-

shore ADCP currents from the ASPEX data campaign (Le Boyer et al., 2013; Kersalé et al., 2016). The location of the data points used for the model assessment are shown in Fig. 1.

### 2.3. Numerical simulations summary

For this study, 4 simulations are completed over the same period of time (October 2010–December 2012):

- A reference simulation, with the configuration described in section 2.1, hereafter REF
- A simulation without tidal forcing, hereafter NOTIDES
- A simulation without the river freshwater discharges, hereafter NORIVER
- A simulation forced with filtered winds (30-days moving average), hereafter WIND30D

For the sake of consistency, surface pressure is also filtered with a 30-day moving average in the WIND30D simulation. The NOTIDES and WIND30D simulations are used to estimate the impact of tides and of the wind variability on the river plume properties, through their direct impact on the plume dynamics or their influence on the shelf hydrology and circulation. The NORIVER simulation allows us to evaluate the river discharge influence on the shelf circulation.

Due to the initialization of the simulation with the IBIRYS solution, the results from NORIVER will only be interpreted and compared to other simulations after a period of 9 months. For REF, NOTIDES and WIND30D, a spin-up of 3 months is considered. Therefore, the period of study spans two full years (2011–2012) for REF, NOTIDES and WIND30D.

#### 2.4. Plume location and properties: double use of stratification and sea surface salinity

Plumes are usually detected and described using sea surface salinity (Lazure and Jégou, 1998; Kourafalou, 1999; Fong and Geyer, 2001; Nash et al., 2009; Liu et al., 2009; Li and Rong, 2012), tracers (Wang et al., 2014; Nguyen-Duy et al., 2021) or chlorophyll or turbidity levels (Chen et al., 2017; Petus et al., 2014; Costoya et al., 2017; Gangloff et al., 2017; Constantin et al., 2018). The criterion based on SSS is the most natural a priori, but choosing a threshold value that remains meaningful for all the hydrological regimes is uneasy. A standard threshold for the Gironde plume would be  $SSS < 33$ . Raising the SSS threshold to 34 would mean having a very thin difference between seawater and plume waters and may lead to an overestimated plume extension at some periods. Here, we propose to use another variable to complement SSS, well known in estuarine studies (Valle-Levinson, 2010; Geyer and MacCready, 2014): the stratification index (Hansen and Rattray, 1966), hereafter “SI”.

$$SI = \frac{(S_{bottom} - S_{surface})}{\bar{S}_z}$$

Where  $S_{bottom}$ ,  $S_{surface}$  and  $\bar{S}_z$  are the salinity at the bottom, the surface and the salinity averaged over the water column respectively.

The use of stratification in addition to the SSS criterion will allow us to detect parts of the plume where SSS is higher than 33 but where the stratification is significant enough to characterize the area as part of the plume. This will essentially happen in the far-field region of the plume. Furthermore, this index will allow us to comment on the state of the waters leaving the estuary (stratified, partially mixed or well-mixed) and within the plume.

The SI threshold is fixed at 4% (0.04). For example, for a 35 salinity at the bottom and a 34.6 mean vertical salinity, the surface salinity would be 33.6. This threshold was chosen after comparing monthly maps of SSS and SI, to determine the value that seemed to be the best representation of the Gironde plume dynamics. Other plumes would not necessarily be well described by this value.

### 3. Model assessment

This section presents the results of model assessment for the REF simulation.

#### 3.1. Tidal elevations

RMS complex errors are calculated for 6 tidal constituents (M2, S2, N2, K1, O1 and M4) and compared to the two datasets available: tidal gauges and satellite altimetry data (Table 1). 52 tidal gauges are used for this assessment. Errors are all given in cm and calculated with the following formula:

$$H_s = \sqrt{h_1^2 + h_2^2}$$

$$h_1 = H_m \cos(G_m) - H_o \cos(G_o)$$

$$h_2 = H_m \sin(G_m) - H_o \sin(G_o)$$

$H_s$  is the complex error,  $H_m$  and  $G_m$  are the modelled amplitude and phase respectively, and  $H_o$  and  $G_o$  are the observed amplitude and phase. Errors are calculated for each constituent.

These errors are higher for tidal gauges than for satellite altimetry because gauges are mainly located in coastal areas where the tidal signal is stronger. Overall, these errors are small (all less than 10 cm) and tides are very well reproduced by the model. In comparison, the mean and maximum amplitudes of M2, S2, K1 and M4 (the four main constituents) in the Bay of Biscay are: 136 cm and 210 cm for M2, 48 cm and 77 cm for S2, 7 cm and 7.6 cm for K1, 3.5 cm and 25 cm for M4.

#### 3.2. Temperature and salinity

Comparisons of modelled SSS and SST to the Islands network buoys are summarized by the RMS errors presented in Table 2. The average error on SSS when compared to the gridded monthly SSS product in the Atlantic Ocean is estimated at 0.18, for the years 2011 and 2012.

Salinity and temperature profiles from the CORA-IBI database (Szekely et al., 2017) were also compared to the model. Only profiles located between 44.4°N and 46.5°N and 3°W and 0.5°W, corresponding to an area under the influence of the Gironde plume are taken into account in this comparison. Fig. 1b shows the spatial distribution and number of profiles (log scale) used. In total for the years 2011 and 2012, 884 temperature profiles and 804 salinity profiles were used to calculate RMS errors (Fig. 1). A large number of profiles is located close to the western limit of our defined area. We also see that in the most eastern coastal part of this area, profiles are well-distributed spatially, allowing us to have an evaluation of the model performance in various places of the shelf, representative of different parts of the plume. Errors are small both for the Islands network buoys and for the profiles, which indicates that the model reproduces well the temporal and vertical variations of temperature and salinity.

To illustrate the ability of the model to reproduce temperature and salinity stratification, a few vertical profiles are detailed in Fig. 2. Their location is indicated in Fig. 1b. These profiles show that the model reproduces well vertical gradients of salinity and temperature in the plume area. The shapes of the profiles are globally in good agreement with data, with sometimes an overestimated mixed layer depth (profiles 2011b and 2012c). The observed salinity at the 2012a and 2012b profiles is below 33 at the surface and increases slowly with depth reaching 34 at about 15 m and 10 m respectively. The corresponding simulated profiles are respectively saltier and fresher by about 0.5. The model-data misfit is smaller for the other profiles of Fig. 2. In the simulation, the surface layer is well mixed in the first 8–15 m (depending on the

**Table 1**

Mean complex errors (cm) between the REF simulation and the available data for M2, S2, N2, K1, O1 and M4.

	M2	S2	N2	K1	O1	M4
Tidal gauges	7.97	3.10	1.85	0.91	0.58	2.67
Satellite altimetry	2.84	1.33	0.66	0.45	0.24	1.33

**Table 2**  
Model (REF) - data comparison for temperature and salinity (RMS errors).

	Temperature (°C)	Salinity
Oléron (surface)	0.34	0.39
Houat (surface)	0.39	0.53
Yeu (surface)	0.56	0.39
CORA-IBI (profiles)	0.59	0.12

profiles), which is not necessarily the case in the observations (e.g. 2012a, 2012b).

### 3.3. Currents

ADCP currents from the ASPEX campaign (Le Boyer et al., 2013; Kersalé et al., 2016), are also used to validate the model. These currents are processed to produce daily averaged currents, projected on the along and cross-shore directions as in Charria et al. (2017). The same processing is applied to the currents extracted from the model. RMS errors are calculated for each component and each station, 9 in total for our simulation period. The average RMS error is 4.72 cm/s for along-shore currents and 2.57 cm/s for cross-shore currents. On average the RMS

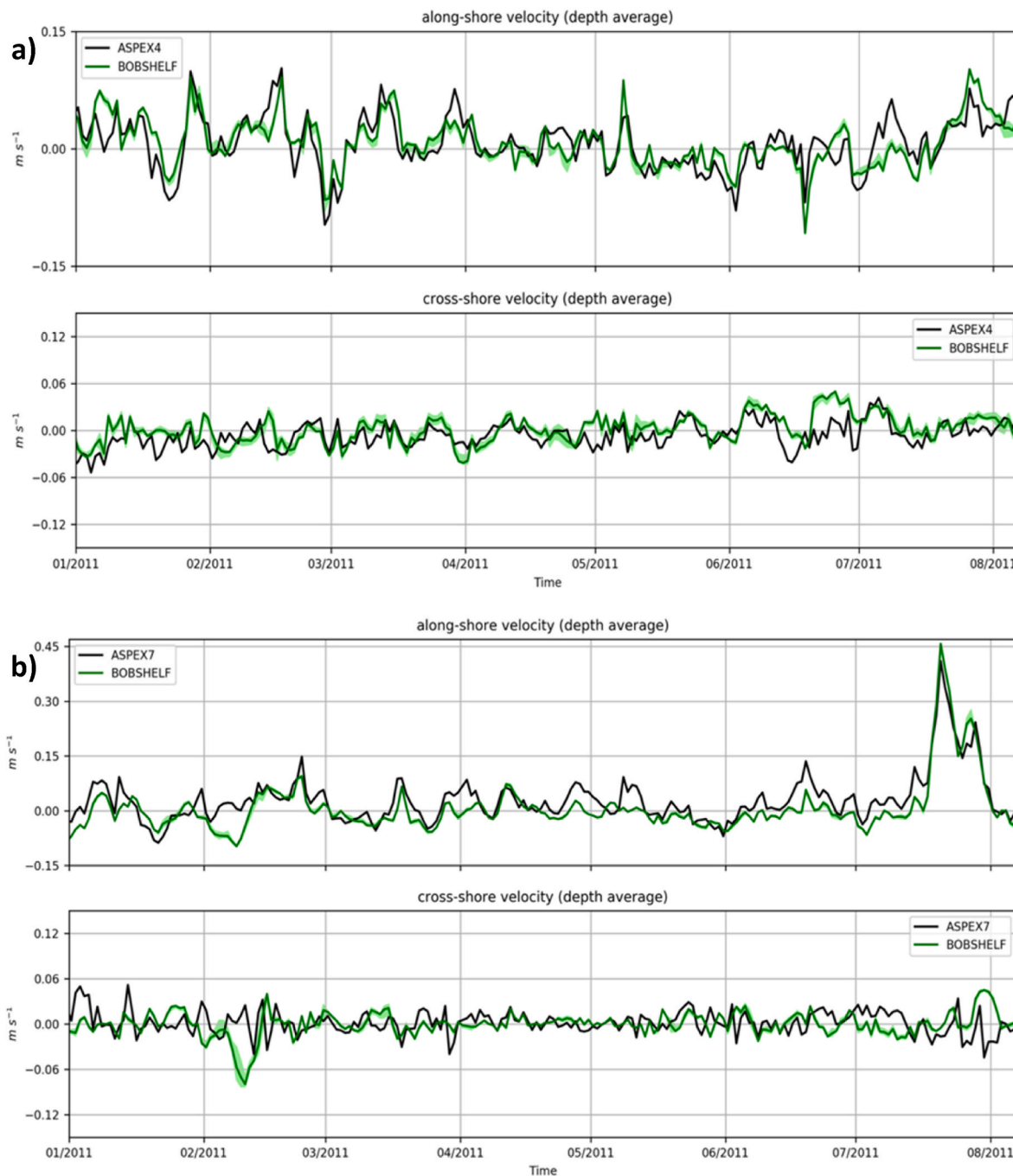


**Fig. 3.** Model (REF) - data comparison with ADCP depth-averaged currents (m/s) in the along-shore and cross-shore directions at 2 locations: a) ASPEX4 (46N52', 2W58'), b) ASPEX7 (44 N, 1W31').

is very close to the mean absolute current for each component. However, a large variability in time is observed with periods of weak and highly variable currents where the model current is not necessarily in phase. In periods where the current increase the relative error is weaker. This is illustrated for example in Fig. 3 which shows the comparisons for the ASPEX4 (~47 N, 3 W) and ASPEX7 (44 N, 1.5 W) moorings, located on the shelf, respectively north and south of the Gironde estuary (see Fig. 1a). In this figure, the grid point co-located to data is represented (solid line), as well as the 4 other closest grid points (shaded area). This “fuzzy verification” allows to compensate for the fact that high-resolution models can perform poorly in single-point comparisons with data while they are actually very accurate (Ebert, 2008).

These moorings are not located directly in the Gironde plume area but show the ability of the model to reproduce the current dynamics on the shelf. We see that the errors are the greatest when the currents are the weakest but that the overall representation of currents is very satisfactory, especially for strong current events. The variability of the along-shore and cross-shore currents is globally well reproduced by the model, especially at the ASPEX4 mooring, located north of the Gironde estuary. For ASPEX7, the peak in the along-shore current in mid-July 2011 is particularly well-reproduced. We can also notice that the ASPEX7 mooring is in the vicinity of the Capbreton canyon, a very complex topographic area. In this context, differences between the model bathymetry and the actual bathymetry can generate large differences in currents from one grid point to another. On the contrary, ASPEX4 is in a rather smooth area in terms of bathymetry, with a progressive gradient from the coast to the open ocean. These bathymetric conditions are more representative of the conditions in the Gironde plume area.

#### 4. Characterization of the Gironde river plume

##### 4.1. Runoff, tides and wind forcing conditions

We first describe the general bathymetry at the estuary mouth and the forcing conditions over the study period. Two sections can be considered as the mouth of the Gironde (solid gray lines, Fig. 1c): a first one across from Royan (hereafter Royan section), and a second one across from the La Coubre cape, through the Cordouan lighthouse (hereafter Cordouan section). The Royan section is characterized by a narrow passage with a central deep channel (up to 30 m depths). The Cordouan section is characterized by a deep channel in the north (up to 28 m depths), a central shallow area (around the Cordouan lighthouse) and a shallow channel in the south (13 m depths maximum).

The top panel of Fig. 4 shows the time series of the sea surface height at the Gironde estuary mouth (Le Verdon, on the Royan section, on the other bank of the river). The low-pass filtered time series of the depth-

averaged current (at the same location) to the cubic power  $\bar{U}^3$  is superimposed to the sea surface height variations and evidences the alternation of spring and neap tides (time series of  $\bar{U}^3$  better represent the contrast between neap and spring tides - see for instance MacCreedy et al., 2009; Nash et al., 2009). The estuary is macrotidal with tidal amplitudes at Le Verdon ranging from 1.5 m during neap tides to 5 m for spring tides. The neap-spring cycle displays monthly modulations, which are likely due to the moon perigean-apogean effects, that is the M2-N2 interactions, as explained for instance in Byun and Hart (2020). Indeed, the main semi-diurnal constituents are M2, then S2 and N2. The typical tidal amplitudes are 1.6 m (M2), 0.54 m (S2), 0.32 m (N2) at Le Verdon.

The mean runoff calculated over 2 years is 550 m<sup>3</sup>/s (480 m<sup>3</sup>/s in 2011, 630 m<sup>3</sup>/s in 2012), with long periods of very low runoff (below 300 m<sup>3</sup>/s). Floods are visible in the runoff time series, the highest ones occurring in spring 2012 (more than 3000 m<sup>3</sup>/s). Interestingly these flood events seem to have an effect on the tidal current velocities since the spring/neap tides contrast is much reduced with respect to the periods with lower discharge (see top panel of Fig. 4). This effect is also noticeable for the winter floods of the end of 2011 and beginning of 2012. A harmonic analysis of the bottom currents was performed over two 3-month periods, for high runoff (April–June 2012) and low runoff (August–October 2011) conditions. The resulting M2 tidal ellipses at the outlet (not shown) are strongly altered between the two periods: in the northern part of the outlet (corresponding to the outflow), the eccentricity is increased from 0.015 (low runoff) to 0.045 (high runoff) close to the La Coubre cape in the deepest part of the channel and from 0.12 to 0.21 just seaward of the Royan section. In this area, the M2 semi-major axis decreases with differences up to -16% (more than 8 cm/s). The semi-minor axis either increases or decreases with differences up to 5 cm/s, which is of the order of the semi-minor axis in itself. The semi-major axis direction also changes with differences of 5°–10°. These results confirm that the M2 tidal currents can be strongly altered by high runoffs, both in direction and amplitude.

The wind is characterized by a large variability (speed and direction) at time scales of a few days (Fig. 4). The largest speeds (>12 m/s) are reached between November and February, but wind bursts are also observed in spring and fall, like, for instance, in May 2012 concomitantly with a flood event. The wind rose of Fig. 5 indicates that the wind is mostly from the west and west-southwest, reaching speeds larger than 15 m/s occasionally, and from the north and northwest, consistently with previous description in the literature (e.g. Le Boyer et al., 2013). Winds from the south and southwest are less frequently observed, but when observed may reach speeds as high as 12.5 m/s. Winds from the southeast have the same frequency of occurrence but do not exceed 10 m/s. Winds used for the WIND30D simulation are also presented in Fig. 5. The applied filtering results mostly in a drastic decrease of both

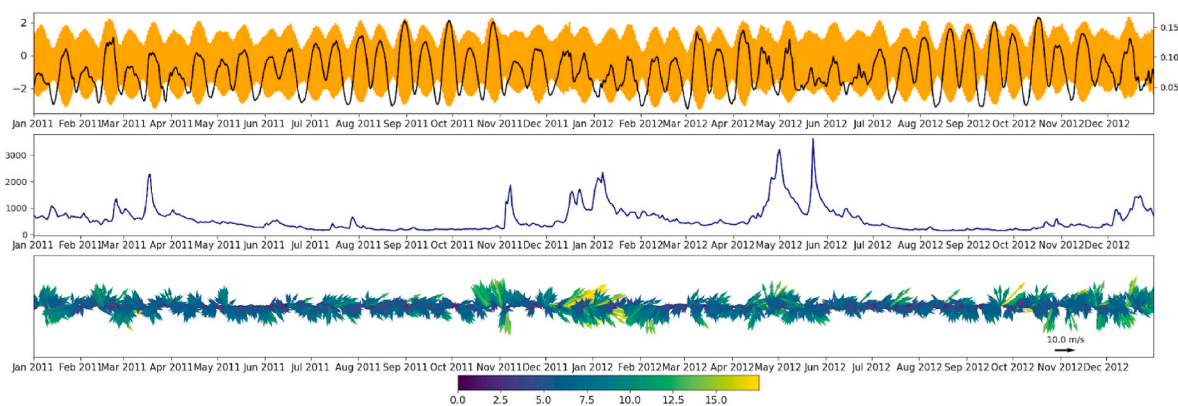


Fig. 4. Main forcings during the simulation period (2011–2012). Top: hourly SSH (m) in orange and low-pass filtered  $\bar{U}^3$  (m<sup>3</sup>/s<sup>3</sup>) in black at Le Verdon (river mouth). Middle: Gironde River discharge (m<sup>3</sup>/s). Bottom: wind at 10 m (m/s) from the ECMWF operational analyses (spatial mean in the 2°–1.125° W and 45°–46° N area).

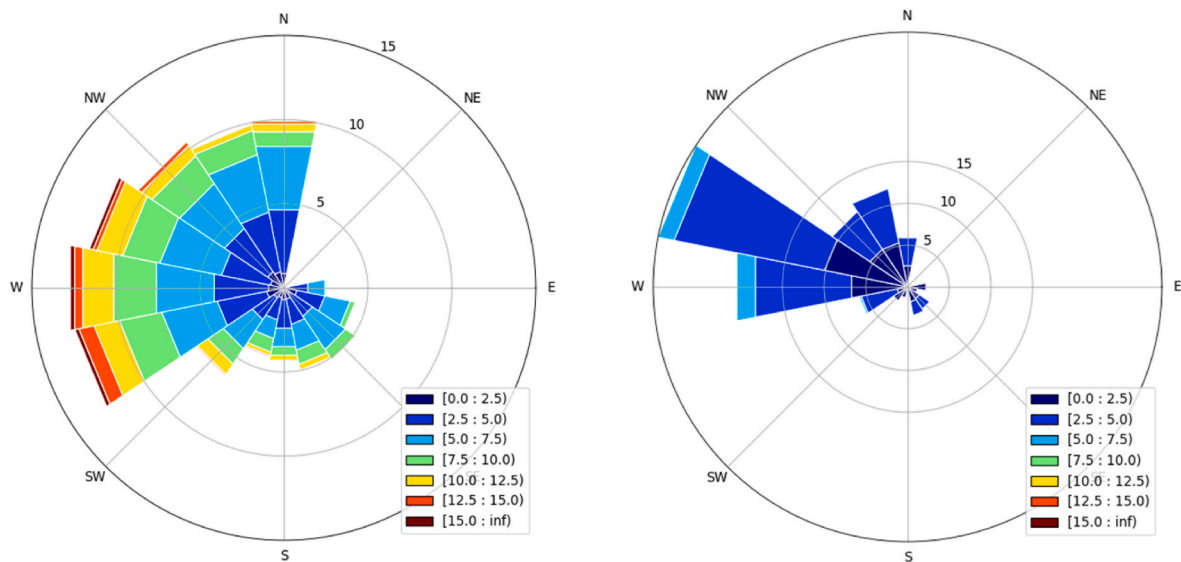


Fig. 5. Windroses of the 10 m wind (m/s) for the 2011–2012 years from the ECMWF operational analyses (spatial mean in the  $2^{\circ}$ – $1.125^{\circ}$  W and  $45^{\circ}$ – $46^{\circ}$  N area) for the REF (left) and WIND30D (right) simulations.

the intensity of winds and the variability of their orientation. In WIND30D, the winds come mostly from the west, and reach maximum values between 5 and 7.5 m/s.

#### 4.2. Mean characteristics of the river plume

Daily means of sea surface salinity (SSS) and of detided surface velocity currents are averaged over 2 years of simulation, after a spin-up of 3 months (Figs. 6a and 7a). Following the criteria of  $SSS = 33$  for the plume limit, these figures show a rather small plume that remains close to the coast, on average. The most seaward extension is obtained in the prolongation of the estuarine channel, around  $45^{\circ}N40'$ . The round shape of the SSS contours at this latitude is due to the intermittent occurrence of a bulge as detailed later in this paper. On the shelf the stratification is relatively weak on average ( $SI < 0.1$ ), with the highest value corresponding to the round shape of SSS. At the Royan section it exceeds 0.1. In contrast, at the Cordouan section it is close to zero (except in the northern deep channel), suggesting that the waters in the southern part of the section are strongly mixed locally and possibly mixed with shelf water. The occurrence frequency of the plume is defined at each point by the ratio of days when the SSS is lower than 33 over the total number of days and is shown in Fig. 6c. The highest occurrence of the plume is observed on the inner shelf, just outside the estuary and north of it. Other regions are characterized by a small occurrence frequency ( $< 0.1$ ).

Surface velocity currents (Fig. 7a) are the strongest at the estuary outlet where the specific bathymetry and morphology strongly constrains the dynamics (Fig. 1c). This configuration creates the conditions for a specific pattern of circulation with, in particular, an intense outflow (up to 35 cm/s) in the deep northern channel south of La Coubre. We also observe several vortices that we discuss in the next section. North of the estuary, a weak and narrow northward current ( $\sim 3$ – $4$  cm/s) flows along the coast of the Oléron island. South of the estuary, a southward wide coastal current (5–6 cm/s) is modelled. However, this current is not associated with a significant signature in the mean SSS. Actually, this current is not representative of a mean circulation pattern over the 2 years; instead, it occurs in specific conditions as we will see later (section 5). Lazure and Jégou (1998) mention a strong southward current south of the Gironde estuary in June.

The large variability of the forcings at daily and seasonal time scales (Figs. 4 and 5) is expected to generate a significant variability of the flow over the shelf and of the plume shape. Fig. 6d shows the standard deviation of the horizontal transport over the study period. Interestingly,

we observe a strong contrast between the large variability of the transport in the deep channels of the Royan and La Coubre sections and over the shelf with the almost null variability at the outlet between the Royan and Cordouan sections. Over the shelf, the transport variability is locally increased at the seaward edge of the mean plume pattern ( $\sim 1W30 - 45^{\circ}N40$ ), where the salinity front undergoes a large variability.

#### 4.3. Sensitivity of the mean plume characteristics to the forcing

To analyze the relative impact of wind and tides on the mean characteristics of the plume, we compute the RMS of the daily differences (hereafter RMSdiff) of the transport over the 2 years, for the NOTIDES and WIND30D simulations (Fig. 8), and over 1 year for the NORIVER simulation (not shown), with respect to the REF simulation. We have checked that for NOTIDES and WIND30D, comparing the RMSdiff over 2 years or over 2012 only does not lead to different conclusions. The standard deviation (STD) of the horizontal transport is also calculated over the same periods, for the 3 sensitivity simulations (not shown) and are compared to the STD for the REF simulation (Fig. 6d).

These comparisons indicate that at the estuary outlet, the horizontal transport is mostly controlled by tides. The RMSdiff for NOTIDES exceeds  $3.5 \text{ m}^2/\text{s}$  in the Royan and northern channels (Fig. 8a), which is much larger than the variability of the transport itself in the REF simulation there ( $< 2 \text{ m}^2/\text{s}$ , Fig. 6d). It is also by far larger than the RMSdiff for NORIVER all over the zone, and than the RMSdiff for WIND30D. The wind variability has no significant influence on the horizontal transport there (Fig. 8b). This is not trivial a priori because the adjacent shelf itself experiences a strong wind-driven variability as evidenced by comparing the standard deviation of the horizontal transport in WIND30D (not shown) and REF. The horizontal transport in the region just seaward of the main extension of the plume (as identified in Fig. 6c) is significantly different in WIND30D and REF (RMSdiff  $> 1.75 \text{ m}^2/\text{s}$ , Fig. 8b). At last, the region of the coastal current (roughly north of  $45^{\circ}N40'$ ) is under the influence of both tides and wind variability.

Comparing the standard deviation for the different runs (not shown), we found that the main effect of tides is to decrease the variability of the horizontal circulation in the area of study, (except at the Royan section where the variability is slightly lower in the absence of tides). On the other hand, the variability of both wind and discharge tend to increase the variability over the shelf.

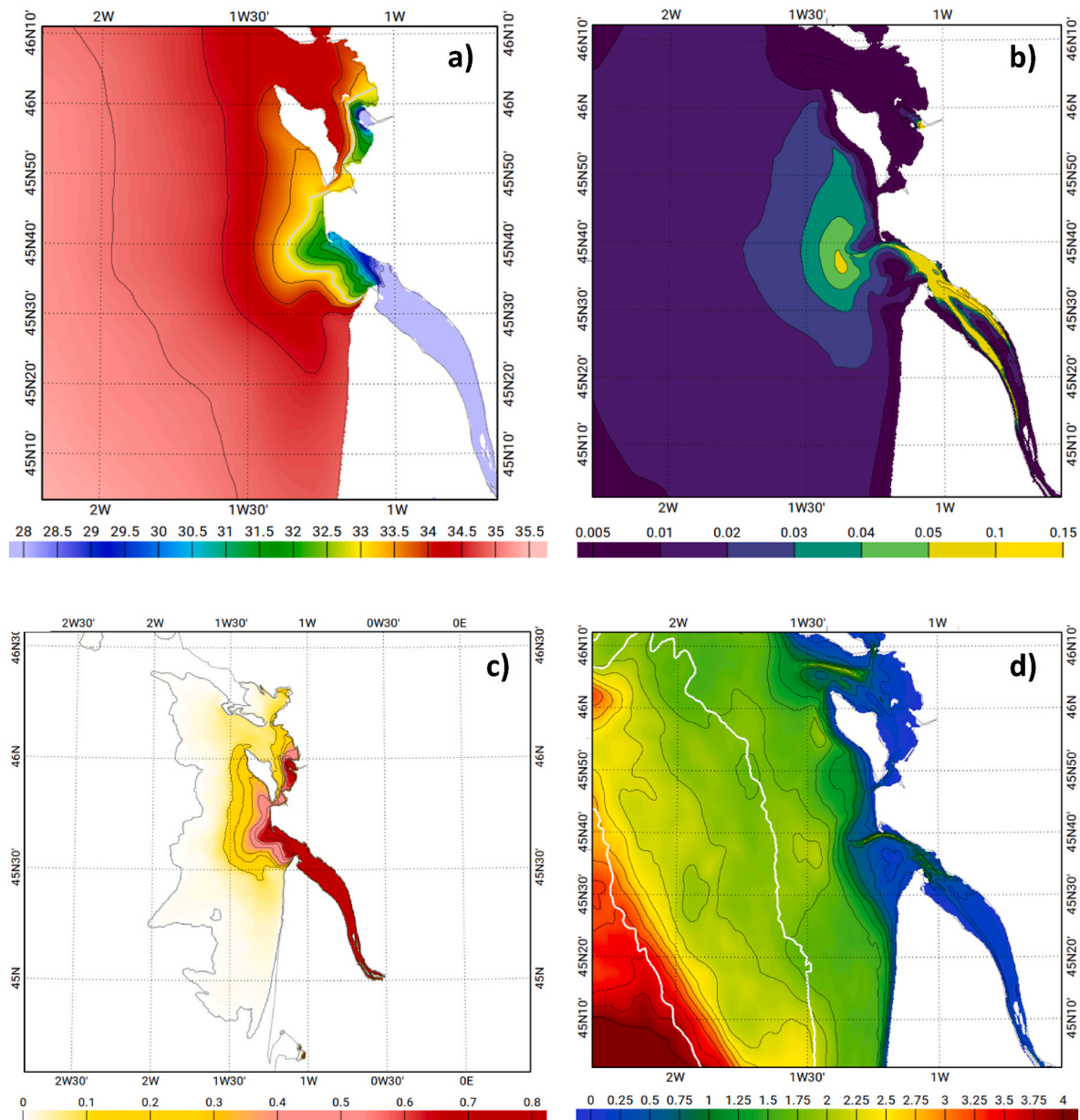


**Fig. 6.** Model results (REF) averaged over 2011–2012. a) Sea surface salinity (in gray: 33 salinity contour), b) Stratification Index (SI), c) Occurrence frequency of the plume (SSS < 33), d) Standard deviation of the horizontal transport ( $m^2/s$ ).

We investigate further the impact of forcings by comparing the mean SSS (not shown), SI and occurrence frequency of the plume in the NOTIDES, WIND30D and REF simulations (Figs. 9, 6a and b, 6c). Both the SSS and the occurrence frequency are strongly impacted by tides, at the mouth and on the shelf, resulting in a very different shape of the plume in the two simulations. In particular, in the NOTIDES run, the plume does not exhibit a round shape as in REF; it expands less seaward and is more elongated along the coast both northward and southward, suggesting that tides tend to prevent the plume from extending southward. As expected, the waters are more stratified in NOTIDES (Fig. 9a) than in REF (Fig. 6b) inside the estuary ( $SI > 0.15$ ), between the Royan and Cordouan section ( $SI > 0.1$ ) and in the plume ( $SI > 0.05$  east of 1W15'). The impact on vertical mixing is further illustrated on a vertical salinity transect (drawn on Fig. 9) in Fig. 10 for the REF and NOTIDES simulations. With tides, vertical salinity gradients are weak in the estuary and at the outlet (including both sections). Without tides, the stratification is much stronger in the estuary and at the two sections of Royan and Cordouan. Over the shelf the thickness of the low salinity

waters is about 10 m in REF. In NOTIDES, the oceanic water ( $S > 34.5$ ) fills the water column below  $\sim 15$  m; the whole section is strongly stratified and the 33 isohaline intercepts the bottom only locally between the two sections.

In contrast, the impact of wind variability on the stratification at the estuary outlet is very weak. The general shape of the SSS contours east of 1W15' (close to the Cordouan section) is not significantly different between REF and WIND30D either. Consistently with what we found for the horizontal transport, the wind impact is much larger over the shelf; the region of stratified less saline waters has a larger extension in WIND30D (Fig. 9b) than in REF (Fig. 6b). The occurrence frequency of the plume is much more distributed over the shelf in all directions (Figs. 9d and 6c). In this area, the mean SSS in WIND30D is lower by  $\sim 0.5$ –1 than in REF; this can be due to both a larger extension of the plume and a decrease in wind-induced vertical mixing, (we cannot exclude the impact of the atmospheric smoothing on heat and fresh-water fluxes at the air-sea interface either). We will see in section 5 the impact of such a change in the hydrology of the shelf on the plume

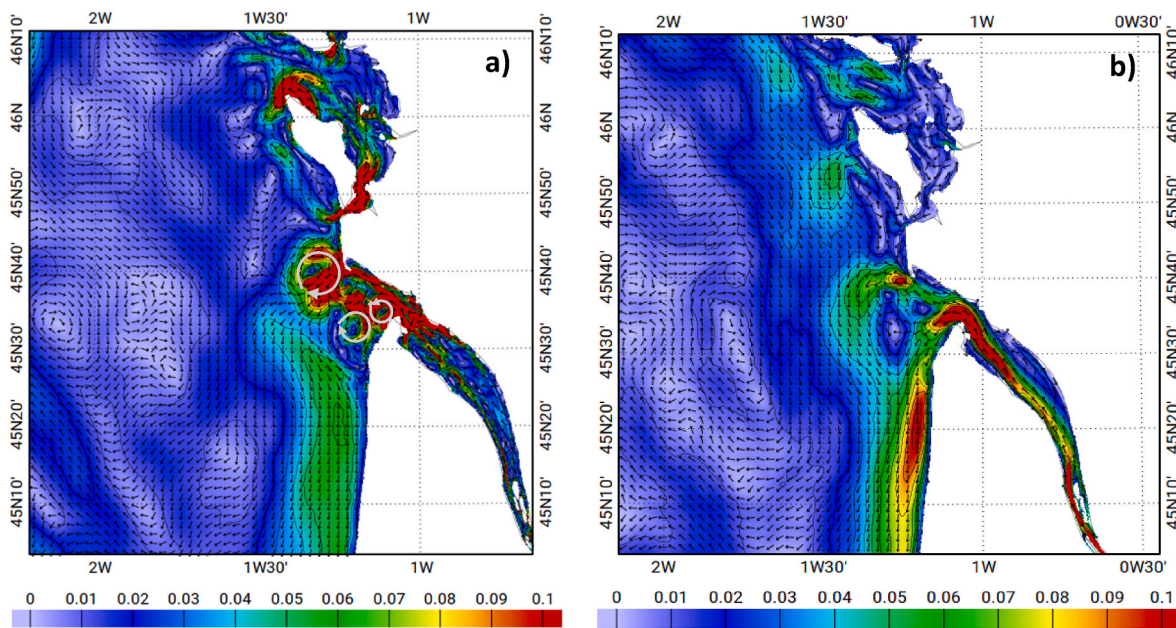


Fig. 7. Surface currents (m/s) averaged over the 2011–2012 years, for the a) REF and b) NOTIDES simulations.

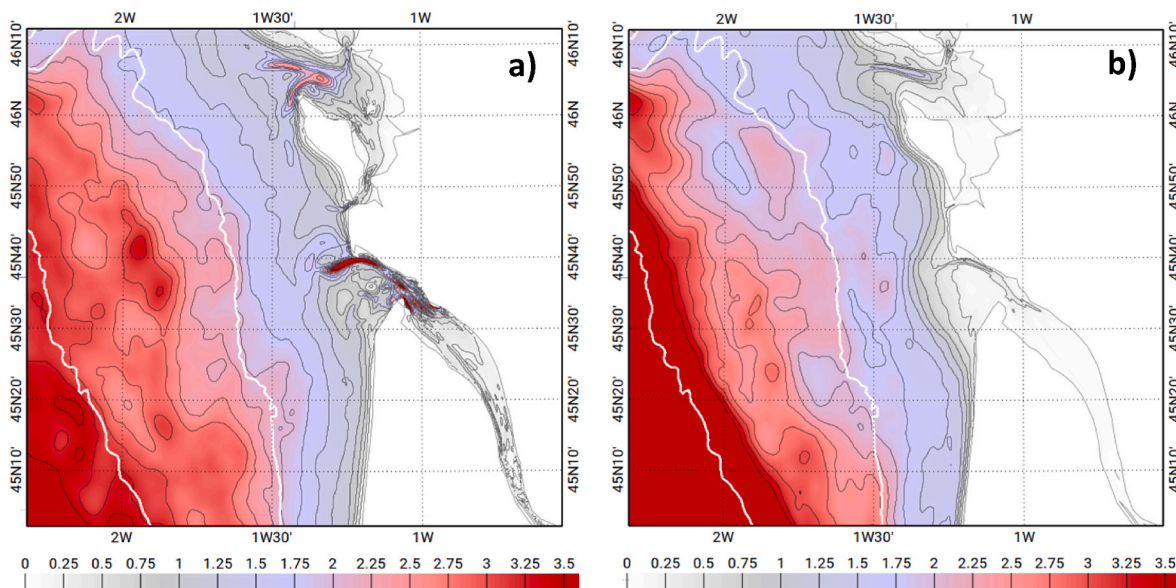


Fig. 8. RMS differences of the horizontal transport ( $m^2/s$ ) between sensitivity simulations a) NOTIDES, b) WIND30D and the REF simulation, calculated over 2011–2012. In white: 50 m and 100 m isobaths.

behavior.

#### 4.4. Impact of tides on the dynamics at the Gironde outlet

Fig. 6c shows that the mean circulation in the area between 1W10' and 1W20' is made of cyclonic and anticyclonic vortices with diameters of about 5 km–12 km. These features are coherent with those observed by Mallet et al. (2000) from a statistical analysis of sediments. In our simulation, maximum currents can reach up to 30 cm/s in the most seaward vortex. In contrast, as mentioned earlier, the variability is very low showing that these are persistent features. Using a 2D tidal model with a constant river discharge, Mallet et al. (2000) suggest that the vortices are residual tidal gyres. To check this hypothesis, we compute the mean surface current over 2011–2012 from the NOTIDES simulation (Fig. 7b). The vortices are not simulated and an outflow is now

noticeable in the southern part of the estuary mouth, of the same order of magnitude as the northern outflow. In the REF simulation (Fig. 7a), this southern outflow does not exist, due to recirculation in this area. Moreover, the southward coastal current is intensified when compared to the REF simulation.

There have been several attempts in the past to characterize the mean dynamics of a plume using characteristic dimensionless numbers, leading to a classification of plumes according to the river discharge, bathymetry, stratification, velocity and geometrical properties at the mouth. One of these numbers is the Kelvin number  $K$  introduced by Garvine (1995), which measures the importance of Earth rotation on the dynamics of the plume. As reported by Wiseman and Garvine (1995) for instance, plumes with  $K \ll 1$  are too small to be impacted by Earth rotation while for plumes with  $K$  close to 1 and larger than 1, Earth rotation will be dominant.  $K$  is defined as the ratio between the across-shore

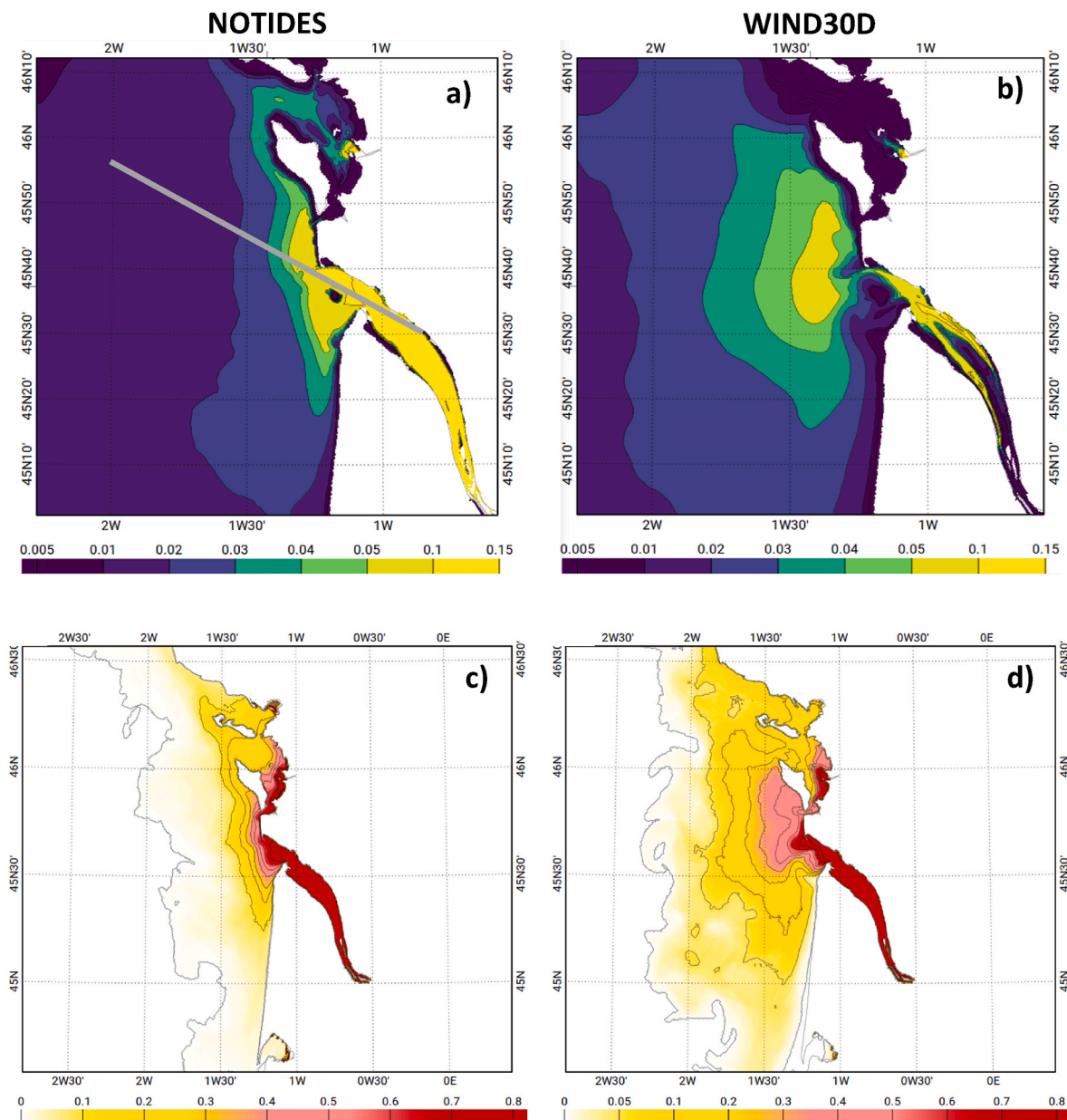


Fig. 9. Averaged SI (top) and occurrence frequency of the plume (bottom) in the NOTIDES (a,c) and WIND30D (b,d) simulations, calculated over 2011–2012. Gray thick line (a): position of transect displayed in Fig. 10.

length scale of the plume ( $L$ ) and the first internal Rossby radius ( $R_d$ ) of the buoyant outflow (see for instance Yankovsky and Chapman, 1997). In this study, we specifically use the formula given by Hetland and Hsu (2013):  $K = fL/\sqrt{(g'h_0)}$  for an outflow of depth  $h_0$ , width  $L$  and density  $\rho_i$  (supposed spatially uniform).  $f$  is the Coriolis parameter,  $\rho_a$  a constant reference density which is representative of the ambient coastal waters and  $g'$  the associated reduced gravity  $g' = g|\rho_i - \rho_a|/\rho_a$ . For the Gironde plume,  $K$  is calculated at the Cordouan section (see Fig. 1) over the 6-month period (January–June 2012) characterized by a river runoff larger than  $400 \text{ m}^3/\text{s}$ . The ambient density is calculated as the mean density over this period and inside a box over the shelf, seaward of the Cordouan section, from the coast to  $2^\circ\text{W}$  and between  $45.33^\circ\text{N}$  and  $46^\circ\text{N}$ . The width of the outflow  $L$  is estimated at 1.6 km from the maps of the mean surface currents. The outflow density is calculated as the mean density over the first two surface levels ( $h_0 = 3 \text{ m}$ ). The resulting difference in density between the outflow and the ambient shelf waters is  $\Delta\rho = 4.4 \text{ kg/m}^3$ . This corresponds to a Rossby radius  $R_d = \frac{\sqrt{g'h_0}}{f}$  of 3.2 km.

This value is consistent with previous estimations on the Bay of Biscay shelves (Charria et al., 2017). The estimated value of  $K$  is  $K = 0.5$ . Thus,  $K < 1$ , which is a condition for a bulge to be formed (e.g. Hetland and Hsu, 2013; Horner-Devine et al., 2015).

In the NOTIDES simulation, the outflow is not constrained to the deep part of the channel and the outflow width is multiplied by four. The inflow depth is kept as  $h_0 = 3 \text{ m}$ , and we find  $\Delta\rho = 4.2 \text{ kg/m}^3$ . The new estimate of the Kelvin number gives  $K = 1.9$ . In this case,  $K$  is no longer less than 1, suggesting that the conditions for the formation of a bulge are no longer met. This is fully consistent with the observations reported in the previous section. We are here in the interesting and specific case where the estuary mouth at the Cordouan section is relatively large, but the ‘effective’ mouth, where most of the discharge flows into the ocean, is reduced to the narrow northern channel. This results partly from the small recirculations or vortices that prevail in the south (Fig. 7a) and limit the outflow through the southern pass. In other words, the vortices are directly impacting the freshwater outflow and therefore the plume characteristics and pathways.

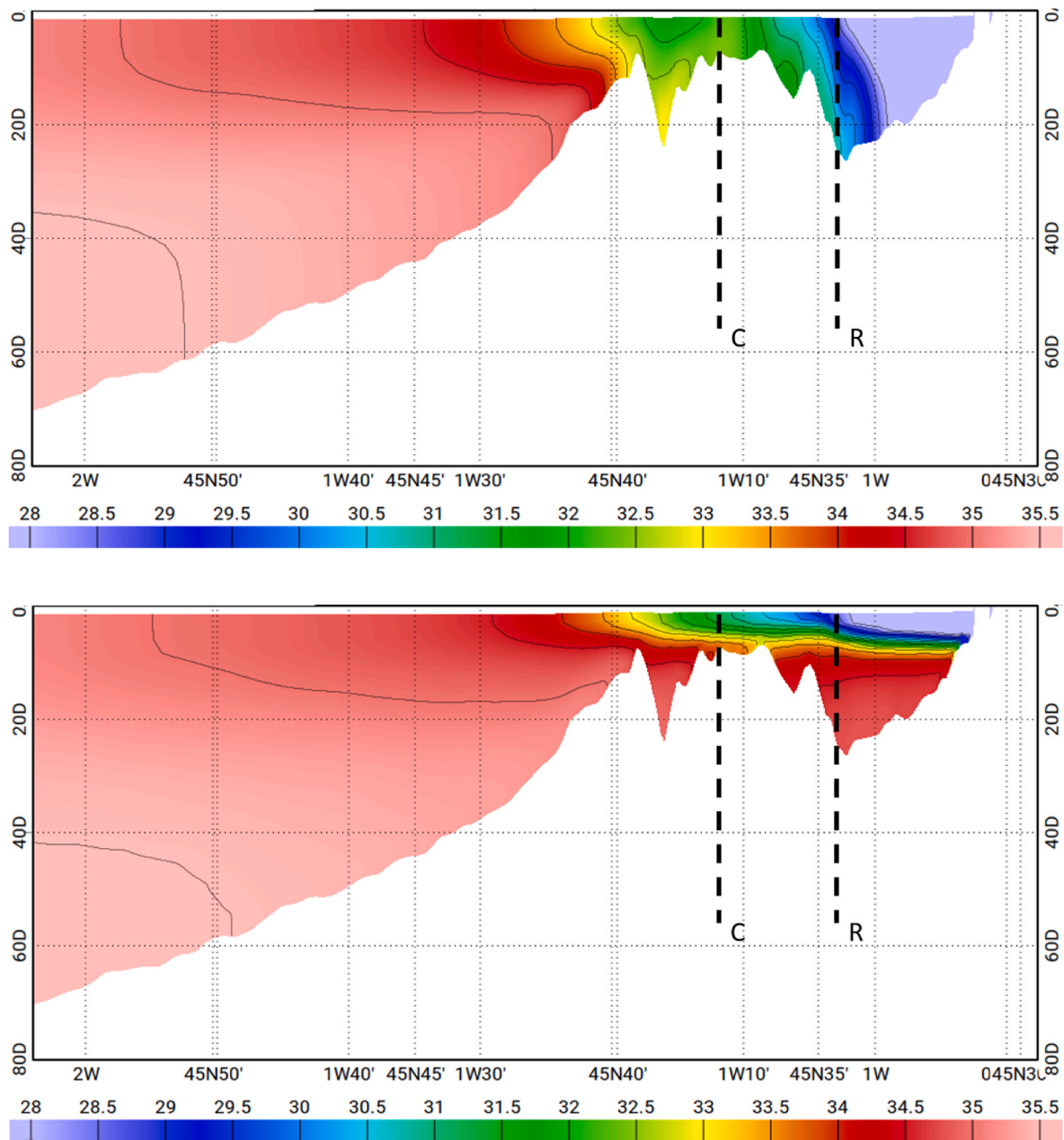


Fig. 10. Vertical transect of salinity (see Fig. 10 for location) averaged over 2 years for the REF (top) and NOTIDES (bottom) simulations. The Cordouan (C) and Royan (R) sections are indicated in black dotted lines.

To conclude, the dynamics in the area between Royan and Cordouan sections (the estuary ‘outlet’) seem to be a key element in the determination of the plume behavior on the shelf. The outlet is similar to a transition zone between the estuary and the plume, where tides modify the stratification of the outflow. But tides also influence the plume through the residual circulation it provokes in this area, resulting from its interaction with the bathymetry. Removing tides in the model changes drastically this circulation. In the next section, we examine in more details the impact of tides (as well as the impact of wind variability) on the plume patterns.

### 5. Plume pathways on the shelf: bulge vs extended plumes

In the previous sections, the Gironde River plume was described and characterized at large temporal and spatial scales. Here, we identify different regimes of the plume based on different characteristics (shape,

extension, intensity of stratification) in the REF simulation. The analysis of daily averages of several quantities (SSS, SI and detided current) over the 2 years of simulation allows us to identify the recurrent occurrence of an intermittent bulge with a circular shape at the estuary mouth, strong SSS and SI horizontal gradients at the edge of the bulge, and a narrow northward coastal current downstream of this bulge. Two other regimes are identified at least twice in our simulation: an extended plume (“EP”), with weaker SSS and SI horizontal gradients and a much larger extension of the plume on the shelf westward and northward; a north-south plume (“NSP”), with a plume extending both northward and southward, and a coastal current southward. Seaward or southward extended plumes in the Gironde have been reported before in the literature (e.g. Lazare and Jégou (1998), Hermida et al. (1998) for a southward extended plume). We also compare these patterns in the different sensitivity simulations in order to better understand the role of the different forcings. The calculations and comparisons are based on

averages of the surface current, the SSS and the SI over the periods for which the plume patterns have been identified. These averages are computed from daily detided files.

### 5.1. Intermittent and recurrent bulge

#### 5.1.1. Main characteristics

In the REF simulation, the bulge and the associated northern coastal current are intermittent features. Five periods characterized by the presence of a bulge have been identified both in winter and spring. In each case, the bulge lasts for 8–13 days. Most of the previous modelling or observational studies (Froidefond et al., 1998; Hermida et al., 1998; Lazure and Jégou, 1998; Puillat et al., 2004; Costoya et al., 2017) do not mention the occurrence of a bulge for the Gironde River plume. However, figures from Froidefond et al. (1998), Hermida et al. (1998) or Lazure and Jégou (1998) exhibit “bulge-like” features. Using an idealized numerical configuration, in a geometric setting similar to that of the

Gironde, Ayouche et al. (2020) find that in condition of high discharge ( $1550 \text{ m}^3/\text{s}$ ) a bulge is formed in the absence of wind and tides and for ambient homogeneous coastal waters initially at rest. They show further that including tides limits the offshore spreading of the plume as found as well by Isobe (2005) in an idealized configuration and by Rong and Li (2012) in the case of the Changjiang River plume for example. In a similar way, Ruault et al. (2020) find that the cross-shore extension of the low-salinity bulge is limited by the action of tides in the case of the Amazon River plume.

In this section, we analyze the bulge observed from March 7 to March 16, 2011. The surface current, SSS and SI all exhibit the characteristic circular shape of a bulge (Fig. 11). The surface current is anticyclonic inside this circular closed pattern and a narrow coastal current is visible north of the bulge, with current velocities reaching on average 20 cm/s at the outer edge of the bulge, and 27 cm/s in the coastal current. SSS and SI show strong lateral gradients from the edge to the center of the bulge, from 34 to less than 31 and from 0.03 to 0.09 in less than 20 km,

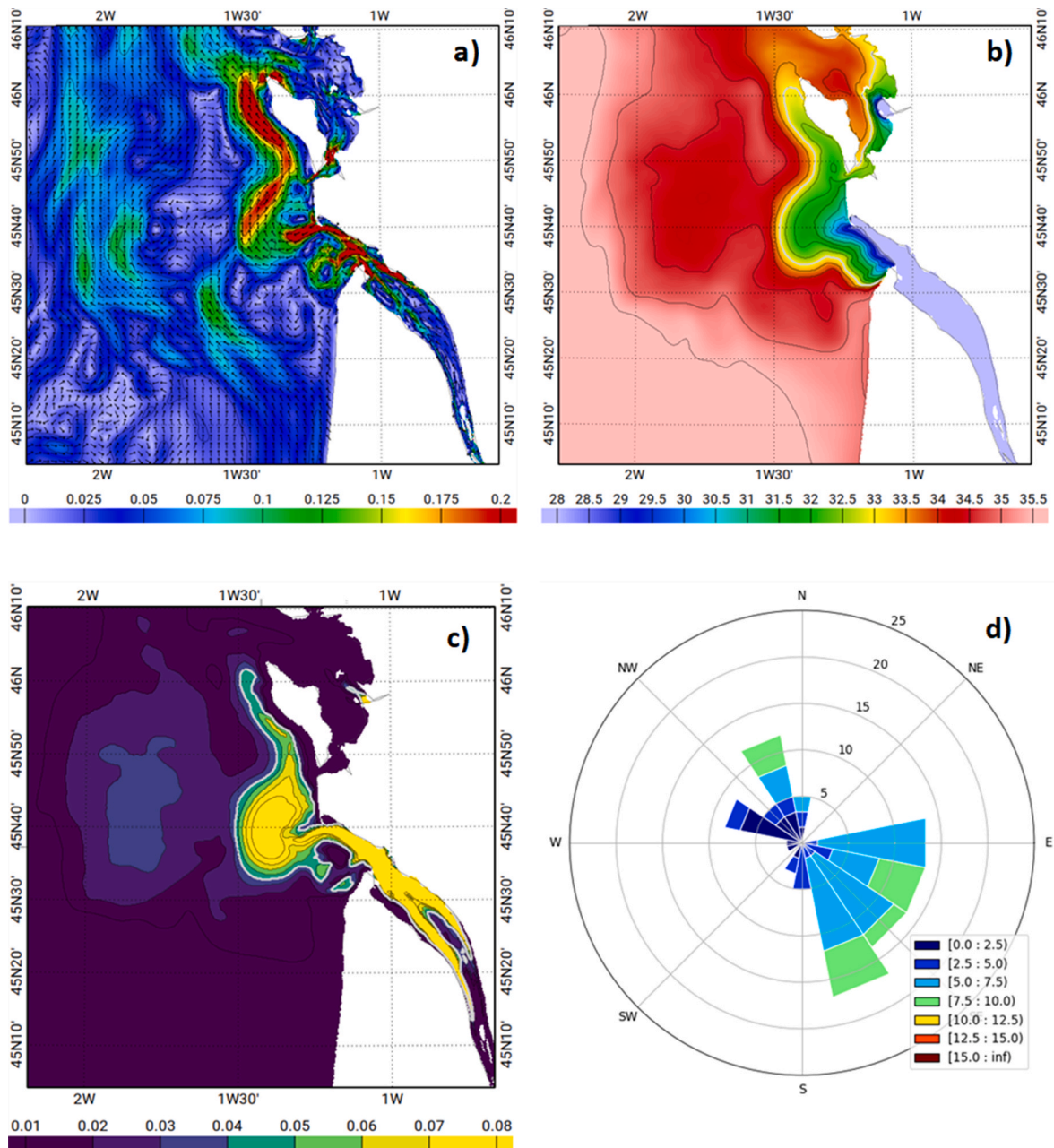


Fig. 11. a) Surface currents (m/s), b) SSS and c) SI for a bulge period (REF run) between March 7 and March 16, 2011.

respectively. Over this period, the mean discharge is  $731 \text{ m}^3/\text{s}$ . The discharge is close to  $600 \text{ m}^3/\text{s}$  during the first seven days (until March 13) then it increases quickly up to  $1476 \text{ m}^3/\text{s}$  on March 16. The winds are mainly south-southeasterly to easterly winds and their speed is relatively low ( $<10 \text{ m/s}$ ). The bulge is formed during the spring to neap transition, intensified in terms of low SSS and strong SI during neap tides (around March 13), and broken down during the neap to spring transition. SI reaches 0.12 in the bulge during neap tides, against 0.09 for the entire period (30% increase).

Further offshore on the shelf, a secondary area of weakly stratified waters is found with SSS between 35 and 34. A northward/northwestward current of medium intensity ( $10\text{--}12.5 \text{ cm/s}$ ) is observed at the edge of this secondary patch of low-salinity waters. The presence of low-salinity waters further offshore is not a systematic characteristic of the bulge events observed in our simulation.

### 5.1.2. Conditions for the bulge formation and destabilization

In the REF simulation, all the bulge occurrences follow the same dynamics with regards to tides: the bulge forms during the spring to neap transition and breaks down during the neap to spring transition. In terms of wind as well, the bulge is characterized by a much less energetic setting than the extended plume and north-south plume. [Hetland and Hsu \(2013\)](#) also note that bulges mainly occur during calm conditions.

In order to better understand the mechanisms at work in the bulge formation and destabilization, we first analyze the situation in the NOTIDES and WIND30D simulations ([Fig. 12](#)). In the NOTIDES run, the SSS and SI during the same period in March 2011 show different patterns: a tongue of SSS lower than 28 extends from the Royan section to the Oléron Island and the area along the coast is globally less salty in surface than in REF ([Fig. 12c](#)). As expected, the stratification is higher ([Fig. 12e](#)). The mean surface currents exhibit a very different behavior from REF as well, with a wider coastal current, and no anticyclonic closed cell ([Fig. 12a](#)). The bulge is no longer visible. Interestingly, although the bulge situations are observed in low wind conditions, the results of the WIND30D simulation ([Fig. 12b,d,f](#)) suggest that without high-frequency wind variability the bulge is 'slack' or replaced by a plume that spreads in the offshore and in the north-south directions.

We interpret all these results in the following way. In the absence of tides, the 'effective' width of the estuary mouth is larger (as described in section 4.4); Earth rotation plays a more important role (the Kelvin number  $K$  is larger than 1) and the outflow is deflected to the right and forms a downcoast coastal current without creating a bulge. The outflow turns to the north forming an anticyclonic pattern, which is not a closed cell as in the case of a bulge, and a strong front is observed.

In the case of weak winds with a low variability, we propose the following explanation referring to the dynamical framework proposed by [Yankovsky and Chapman \(1997\)](#) which states that, when formed, the bulge is in a cyclostrophic balance (their equation 6). The pressure gradient force involves the reduced gravity associated to the difference of buoyancy between the estuarine outflow and the ambient shelf waters. In the WIND30D simulation, the shelf waters have a lower salinity than REF on average and are more stratified ([Fig. 9b](#)) (see section 4.3) likely because of a weaker vertical mixing. The occurrence frequency of the low salinity contour  $\text{SSS} = 33$  in [Fig. 9d](#) also shows that low salinity surface waters are more frequently observed offshore, southward and northward than in REF. The density difference between the estuarine outflow and the shelf waters is reduced with respect to REF. In other words, the condition for a density front to exist is not met in WIND30D; without a density front, the bulge cannot develop.

Tides also impact the difference of density between the estuarine outflow and shelf waters, through the alternance of neap and spring tides. Neap tides favor the export of freshwater from the estuary to the shelf because of weak mixing. Snapshots of hourly SSS outputs from the model (not shown) clearly show the difference between SSS during spring and neap tides. On the other hand, spring tides are characterized by strong mixing which has a double effect: breaking down the

stratification in the bulge thus allowing for detachment of the plume from the coast; and increased mixing at the estuary mouth, resulting in higher SSS and lower SI. Detachment of the plume in neap to spring transitions following a bulge situation has also been observed in the Changjiang River plume by [Rong and Li \(2012\)](#) or in the Yellow River plume by [Yu et al. \(2020\)](#).

Calculations of the Richardson number can also testify of this transition from a rather stable state (bulge) to an unstable state (detachment) in the plume. [Fig. 13](#) shows the surface Richardson number calculated from hourly outputs of the model, and averaged over 3 days. We take the average over the 3 days that correspond to the lowest tidal coefficient (peak of the neap tidal cycle, from March 13 to March 15, 2011) and over the 3 days that correspond to the period where the tidal coefficients are increasing and changing the fastest (neap to spring tidal conditions, from March 17 to March 19, 2011). A common critical value adopted for the Richardson number ( $Ri$ ) is 0.25 (e.g. [Ayouché et al., 2020](#); [Nash et al., 2009](#); [Tarya et al., 2015](#)). [Fong and Geyer \(2001\)](#) estimate from the literature that the critical Richardson number ( $Ri_c$ ) ranges between 0.5 and 1. If  $Ri < Ri_c$ , the plume is unstable and turbulent. In [Fig. 13](#), white areas correspond to  $Ri > 1$  (stable conditions) and light red areas to  $Ri < 0.25$  (unstable conditions). Snapshots of the SSS at ebb tide (low tide) are also shown for the 15th and the 19th of March. During neap tides (on the 15th), bottom friction and shear are very weak and stratification is strong because both of weak mixing on the shelf and of the input of less mixed estuarine waters; this results in a stable water column with high Richardson number. When tides are increasing (on the 19th), bottom friction is rising, generating some shear in the water column; at the same time, estuarine waters are more mixed. In consequence the Richardson number decreases, triggering instabilities and mixing. The bulge is no longer present and we observe the detachment of a low SSS patch ([Fig. 13d](#)). The southwestern part of the domain is not yet impacted by the estuarine waters ([Fig. 13](#), bottom panel), so the water column remains stable.

Note that when the bulge is formed, an increase of wind could lead to a destabilization of the bulge, through a similar mechanism, that is by generating a large shear and triggering instabilities. This has been observed in one case of bulge in our REF simulation. A systematic study over a larger period of time would be needed to better understand which forcing (increased wind or tides) is more likely to destabilize the bulge.

Thus, both wind and tides play a role in the bulge formation at different time scales. Tides have a direct impact, through the alternance of neap and spring tides. Without tides, a bulge cannot be formed. On the other hand, winds have a role at a larger scale, impacting the characteristics of the ambient shelf waters by advection and/or mixing.

## 5.2. Seaward and north-south extended plumes

### 5.2.1. Seaward extended plume

We examine an example of seaward extended plume (hereafter 'EP') which is observed from January 22 to February 8, 2012 ([Fig. 14](#)). There is no longer an anticyclonic circulation at the river mouth like in the bulge configuration. SSS and SI lateral gradients are a lot weaker, from 34 to less than 31 and from 0.03 to 0.07 in about 35 km, respectively. The discharge oscillates slightly around a mean value of  $722 \text{ m}^3/\text{s}$ ; the minimum (resp. max) discharge over this period is  $600 \text{ m}^3/\text{s}$  (resp.  $866 \text{ m}^3/\text{s}$ ). Surface currents are much weaker than for the bulge (except for the estuary outlet), with maximum values of  $10\text{--}12.5 \text{ cm/s}$ . Along the edge of the plume, surface currents are oriented towards the west/southwest. Along the southern coast, another current of stronger intensity is observed, but does not seem to be associated with a significant transport of freshwater. In the other EP period, there is no southward coastal current.

This EP follows a bulge (between January 13 and 21) as does the other major EP episode observed during our study period. As seen in the previous section, one mechanism responsible for the relaxation of the bulge is an increase in vertical mixing, either due to stronger tides

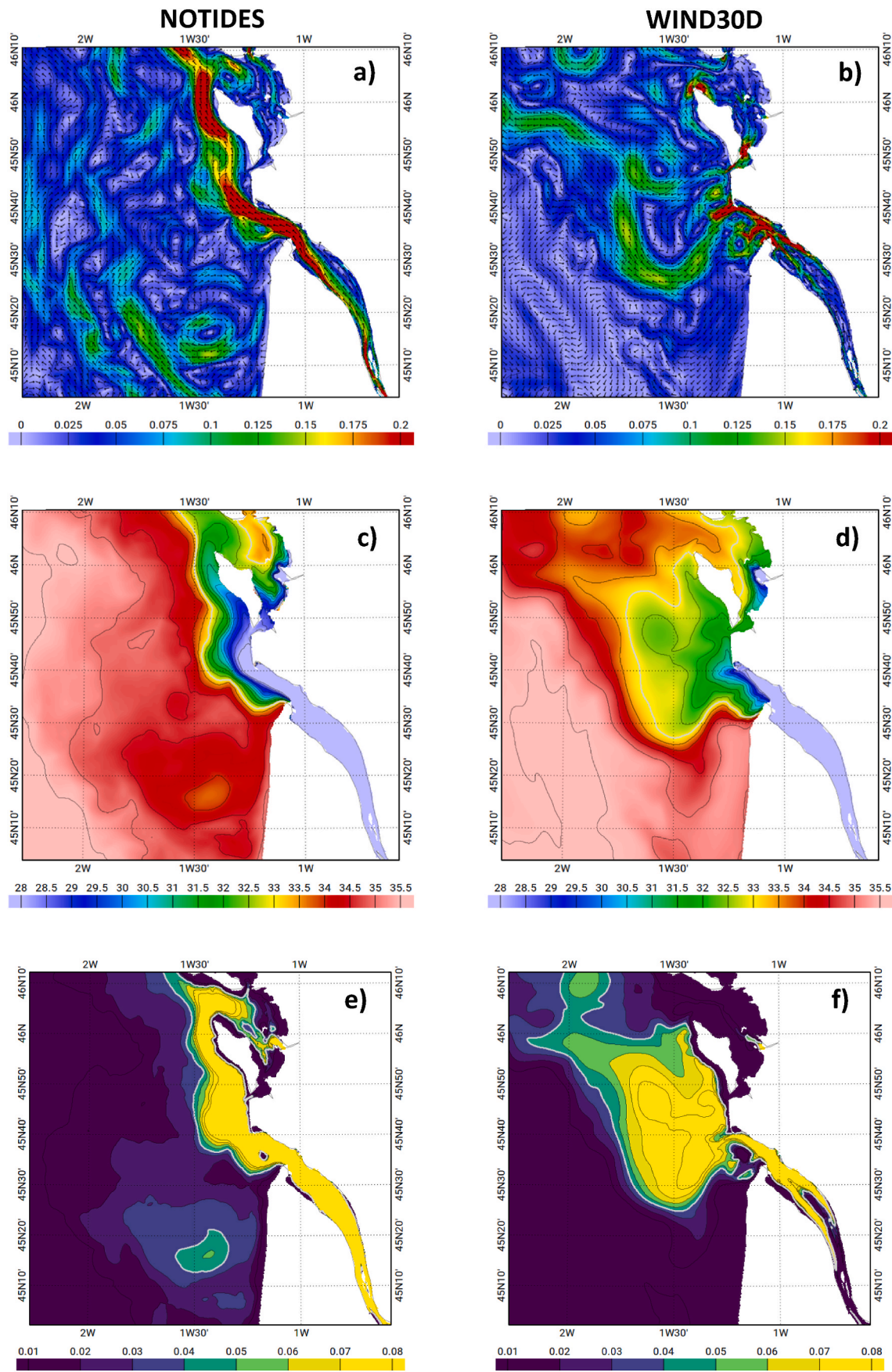
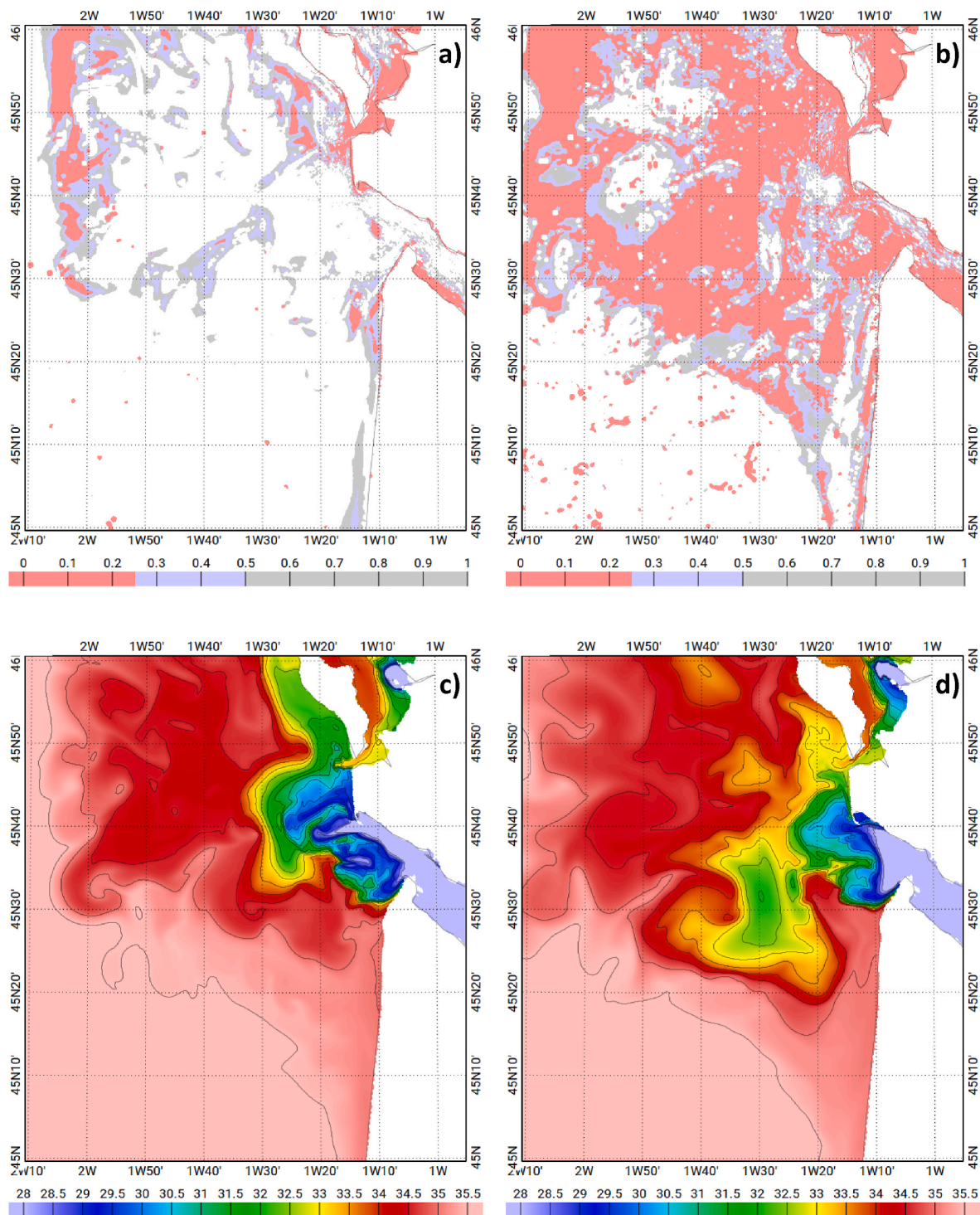


Fig. 12. Surface currents (m/s) (top), SSS (middle) and SI (bottom) for the same period as Fig. 11 (bulge period) in the NOTIDES (a,c,e) and WIND30D (b,d,f) simulations.



**Fig. 13.** Surface Richardson number averaged over 2 periods of 3 days: a) 03/13/2011–03/15/2011; b) 03/17/2011–03/19/2011. In white: stable conditions ( $Ri > 1$ ); in red: unstable conditions ( $Ri < 0.25$ ). Instantaneous SSS at ebb tide on c) March 15, 2011 (bulge) and d) March 19, 2011 (no bulge).

(spring tides) or stronger wind. In this example, winds are coming from the north/north-west and reach higher values (up to 14.3 m/s) than during the preceding bulge period (maximum winds of 9.4 m/s) and than during the bulge case described in the previous section (maximum winds of 9.8 m/s). The wind direction during the EP period is favorable to upwelling, which is a factor favoring plume extension (Hetland and Hsu, 2013).

### 5.2.2. North-south extended plume

We now examine the case of an extended plume in the north-south direction (hereafter ‘NSP’). For this example, the NSP occurs from December 31, 2011 to January 12, 2012 (Fig. 15). SSS and SI horizontal gradients are strong at the western edge of the plume with variations of the same order as for a bulge. The discharge increases from 937  $m^3/s$  on December 31–2348  $m^3/s$  on January 7 then decreases down to 1163  $m^3/s$  on January 12; the mean discharge is 1627  $m^3/s$ . Winds are coming from the west, and reach the highest values encountered in the three

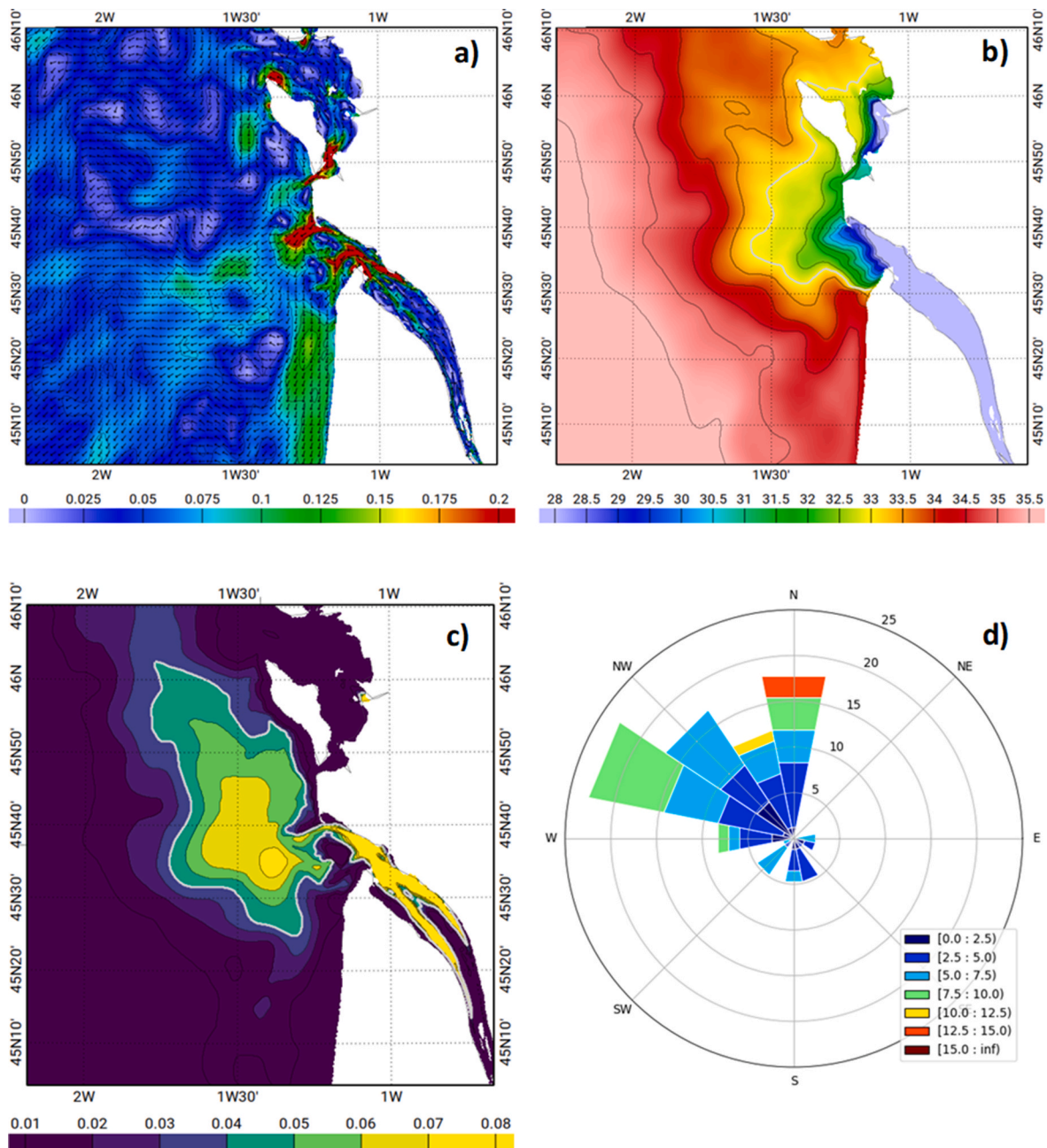


Fig. 14. a) Surface currents (m/s), b) SSS and c) SI for a seaward extended plume (EP - REF run) between January 22 and February 8, 2012. d) Corresponding 10 m winds (m/s) during the same period.

plumes described in this section (more than 15 m/s). This period of NSP is very dynamic, with strong winds at the beginning of the period (more than 12 m/s on December 31st), even higher winds between January 3 and 6 (more than 10 m/s on average with two peaks at 15.5 m/s and 16 m/s), followed by weaker winds until the end of the period (less than 8 m/s). In these conditions, surface currents are also changing rapidly and the representation of averaged currents is not pertinent. We choose to present daily averaged snapshots of January 5 and January 8 (Fig. 15). For January 8, the figure is zoomed in to better analyze the surface currents at the Gironde outlet. On January 5, winds are the strongest and coming from the west/northwest. The corresponding surface currents are strong (>20 cm/s in majority) and oriented towards the south/southeast all over the shelf. Maximum currents reach 35 cm/s just offshore of the estuary outlet. These currents are consistent with the strong westerly winds at this date. They provoke the advection of

freshwater to the south and mixing with shelf waters. On January 8, when the winds are relaxed, currents on the shelf offshore are weak. Maximum currents are then westward and located in the deep channel of the Cordouan section.

### 5.2.3. Joint action of wind and tides

In the EP case, winds are from the north, in a direction favorable to upwelling and to offshore spreading of the plume. In WIND30D, the EP is more extended northward and southward (Fig. 16). This can be explained by the reduction of winds intensity and, consequently, of the Ekman current in the westward direction that was prevailing at ~45N30' (Fig. 14). In the absence of this constraint, the plume is able to spread further northward and southward. Such impact of upwelling favorable winds on the offshore spreading is reported in the literature (for instance, Hetland and Hsu, 2013, Fong and Geyer, 2001).

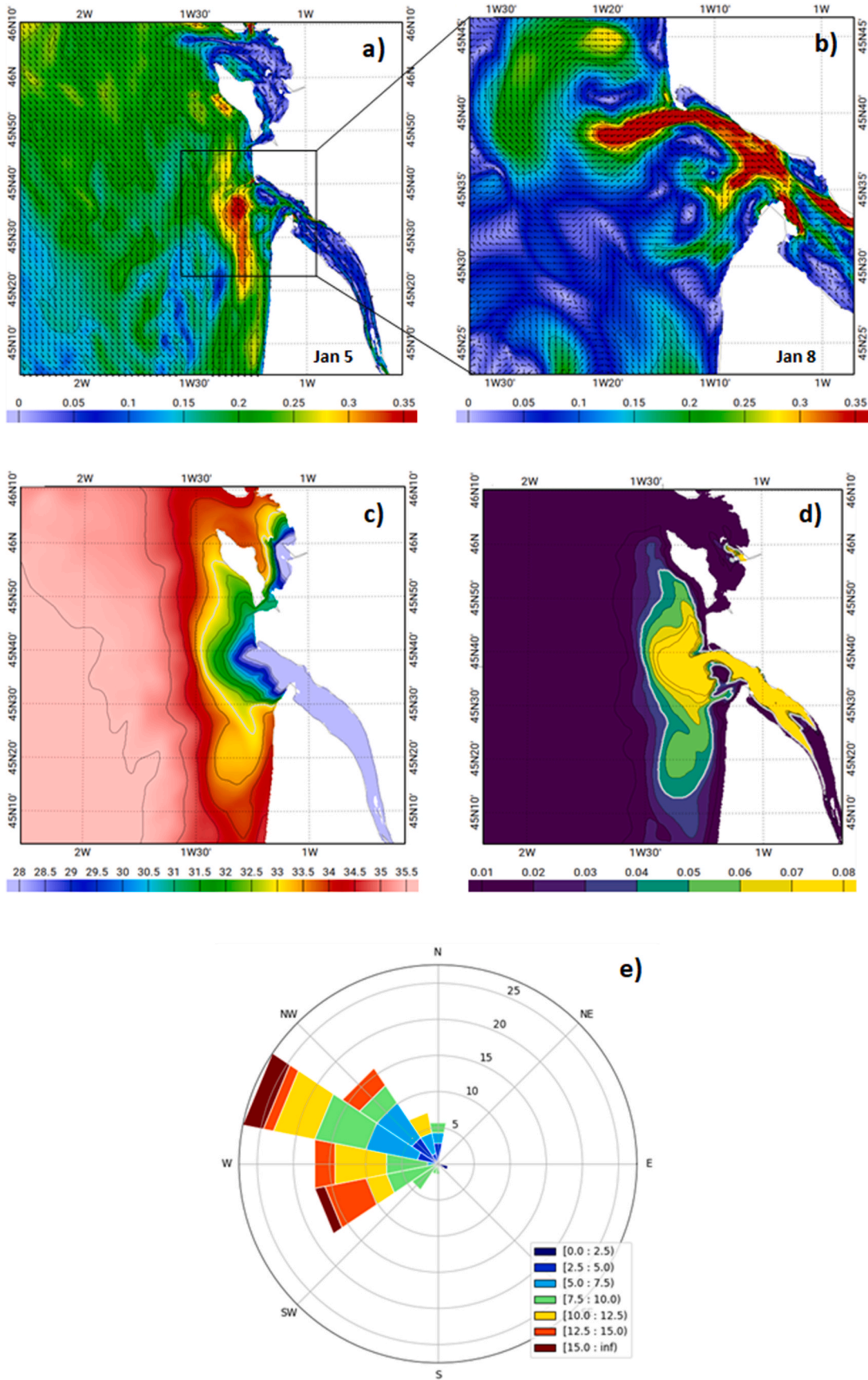


**Fig. 15.** Surface currents (m/s) on a) January 5 and b) January 8, 2012. c) Averaged SSS and d) SI for a north-south plume (NSP), between December 31, 2011 and January 12, 2012 (REF run). e) Corresponding 10 m winds (m/s) during the same period.

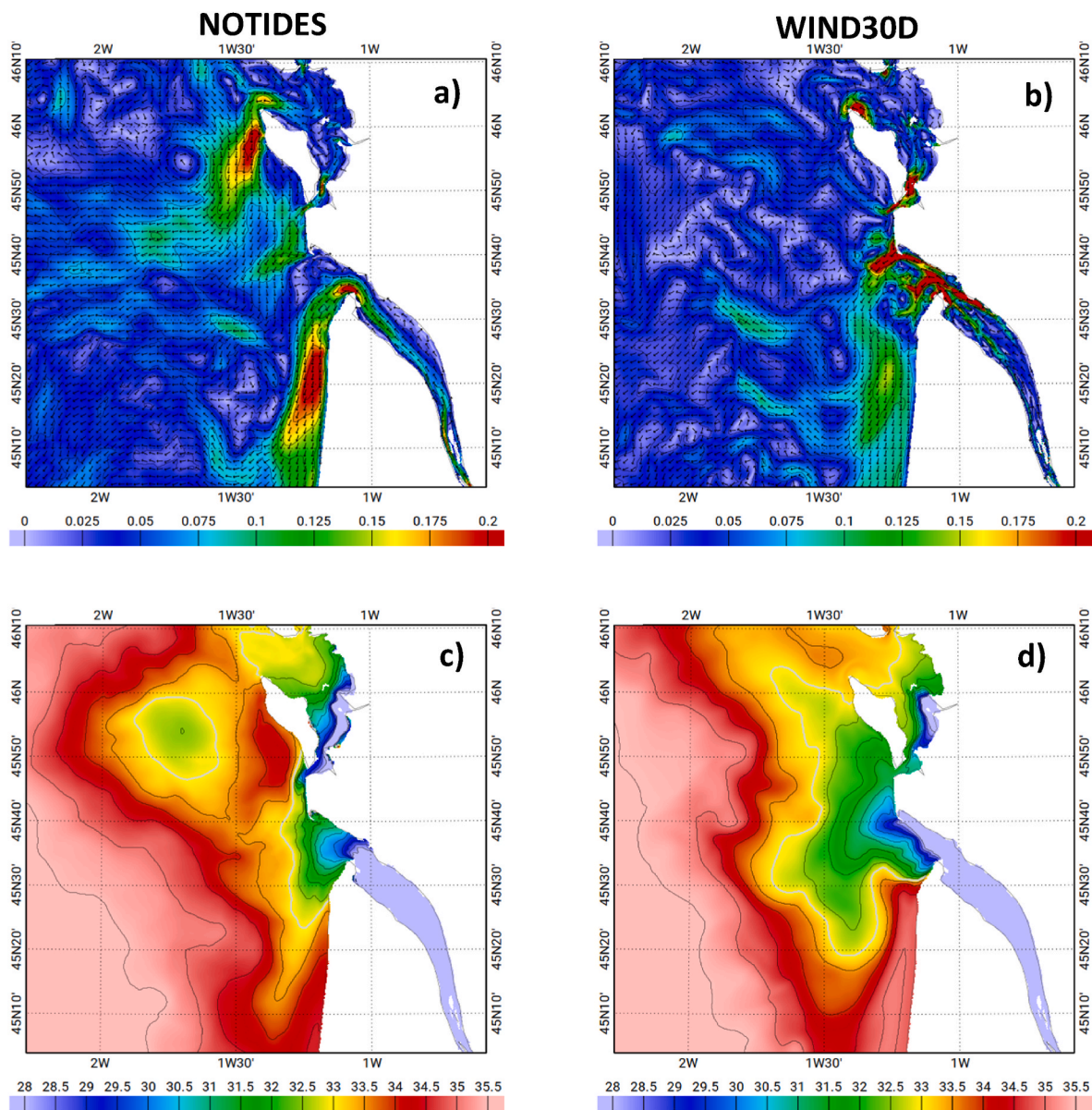


Fig. 16. Surface currents (m/s, top) and SSS (bottom) for the same period as Fig. 14 (seaward extended plume) in the NOTIDES (a,c) and WIND30D (b,d) simulations.

When the plume is spreading southward (NSP case), winds are oriented landward, which is consistent with a southward/southeastward current. The flow of low salinity waters represents an additional geostrophic component which reinforces along the coast the southward Ekman current. In WIND30D, the plume spreads further offshore, and the stratification is also larger within the plume. On January 5, surface currents are much weaker all over the shelf (Fig. 17a) compared to REF (Fig. 15) where a consistent southeastward/southward current of about 20 cm/s is observed between the coast and the mid-shelf (100 m depths). Low salinity waters are then less constrained to the coast and the plume is more extended offshore (not shown). Besides, the wind-induced mixing is reduced (not shown), so the dilution is weaker over the shelf and the freshwater is found further offshore and further south than in REF.

As seen in Section 5.1 for the bulge, tides also participate in shaping the plume. In NOTIDES, for the EP, the detachment of a low salinity cell is observed off the Oléron Island, with a strong signature in surface currents (Fig. 16a). Two effects are combined to obtain this pattern. First of all, in REF, the increase in river discharge is followed by spring tides.

Thus, the increase in freshwater input on the shelf is occurring at the same time as the increase of mixing due to tides. In NOTIDES, the vertical mixing is weaker and the freshwater is maintained at the surface, allowing its spreading further north and eventually its detachment from the coast. In addition, in the absence of tides, the surface circulation over the shelf is characterized by more numerous small-scale patterns. In particular, during the EP period, an anticyclonic pattern develops in the vicinity of the Oléron Island (Fig. 16a) and advects the coastal freshwater offshore.

The river discharge forcing must also be considered. A significant increase in the Gironde runoff occurs at the end of 2011/beginning of 2012 (Fig. 4). As seen in the same figure, this freshwater input has an effect on the  $\bar{U}^3$  estimation, proxy of the tidal forcing: neap/spring oscillations are damped by the discharge. In Section 4, we emphasized the determinant effect of tides on the plume, in particular through its action on residual circulation at the estuary mouth. In Fig. 15b (NSP), the anticyclonic vortex seen south of Cordouan in the long-term average of the surface circulation (Fig. 7a) or during the bulge period (Fig. 11a) is not “closed” on January 8, after the flood peak, meaning that the

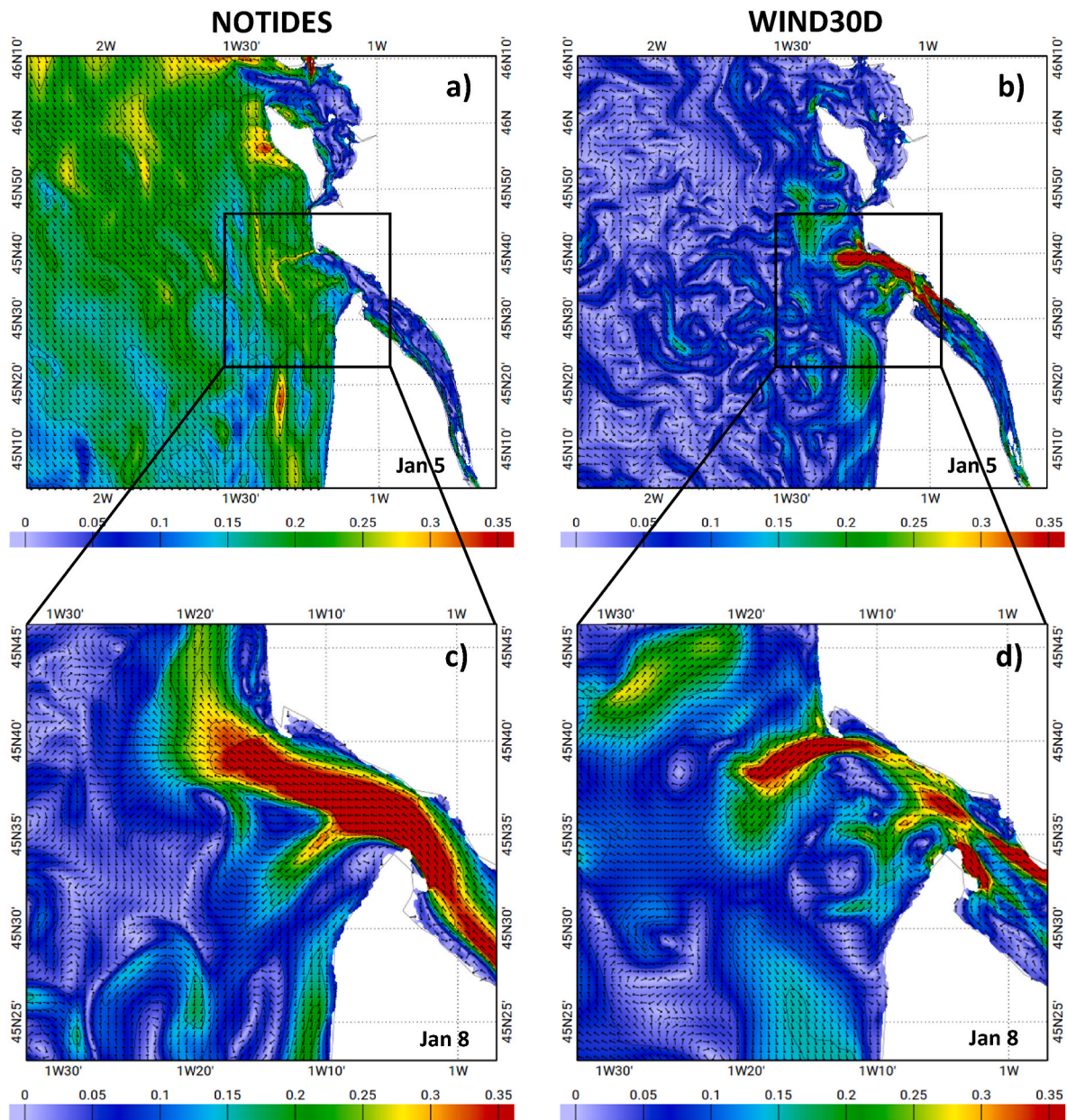


**Fig. 17.** Surface currents (m/s) on January 5 (top) and January 8 (bottom), 2012, as in Fig. 15 (north-south plume) in the NOTIDES (a,c) and WIND30D (b,d) simulations.

recirculation is broken. In NORIVER (not shown), the recirculation south of Cordouan is stable and unbroken, for the same tidal and wind conditions. In NOTIDES (Fig. 17c), the recirculation does not exist and the flow passing to the south is even greater. In WIND30D (with weak winds), this recirculation is not fully closed, as in REF (Fig. 17d). These comparisons indicate that strong winds alone cannot explain the change in circulation in this area. As shown in section 4.1, tidal ellipses are altered at the mouth when the river discharge is strong. We suggest then that a flood, by altering the effect of tides in this area, can favor an opening to a southern exit of freshwater. We have checked that the small recirculation south of Cordouan is systematically altered during a peak of flood. However, this is not a sufficient condition for the plume to spread southward, wind-induced advection in case of westerlies is also necessary

### 5.3. Energy terms

Several terms of the mechanical energy budget are calculated for the REF simulations, following MacCready et al. (2009) and Zu et al. (2014), as an attempt to identify and quantify the main forces at play. The aim here is not to obtain a closed budget, but rather to be able to discuss the relative importance of the following terms: bottom dissipation, internal dissipation, buoyancy term and wind work; in addition to the analysis in section 5.1 and 5.2. The calculations are made according to the following formulations:

$$DISS_{BOT} = -\rho_0 C_D |U_H|_{z=z'}^3$$

$$DISS_{INT} = -\int_z^{\eta} \rho_0 K_M (u_z^2 + v_z^2) dz$$

$$BUOY = -\int_{-H}^{\eta} g K_D \frac{\partial \rho}{\partial z} dz$$

$$WIND = (u\tau^x + v\tau^y)|_{z=\eta}$$

where  $\rho_0$  is a constant background density ( $1025 \text{ kg/m}^3$ ),  $\rho$  the density,  $K_M$  the eddy viscosity and  $K_D$  the eddy diffusivity.  $H$  is the bottom depth.  $C_D$  is the bottom drag coefficient; it follows a logarithmic law (Blumberg and Mellor, 1987), depending upon the bottom roughness length which is set to 1 mm.  $U_H = \sqrt{u^2 + v^2}$  where  $(u, v)$  are the horizontal

components of the total current (i.e. including the tidal current). In the calculation of  $DISS_{BOT}$ ,  $(u, v)$  are taken at the first level above the bottom ( $z = z'$ ). For the computation of the wind work  $WIND$ , we use the surface current (i.e. at  $z = \eta$ ).  $u_z$  and  $v_z$  are the partial derivatives of  $(u, v)$  with respect to the vertical dimension  $z$ .  $\tau^x, \tau^y$  are the wind stress components.

Bottom dissipation ( $DISS_{BOT}$ ) is representative of tidal dissipation while internal dissipation ( $DISS_{INT}$ ) allows us to estimate dissipation by shear inside the water column. The buoyancy term ( $BUOY$ ) is repre-

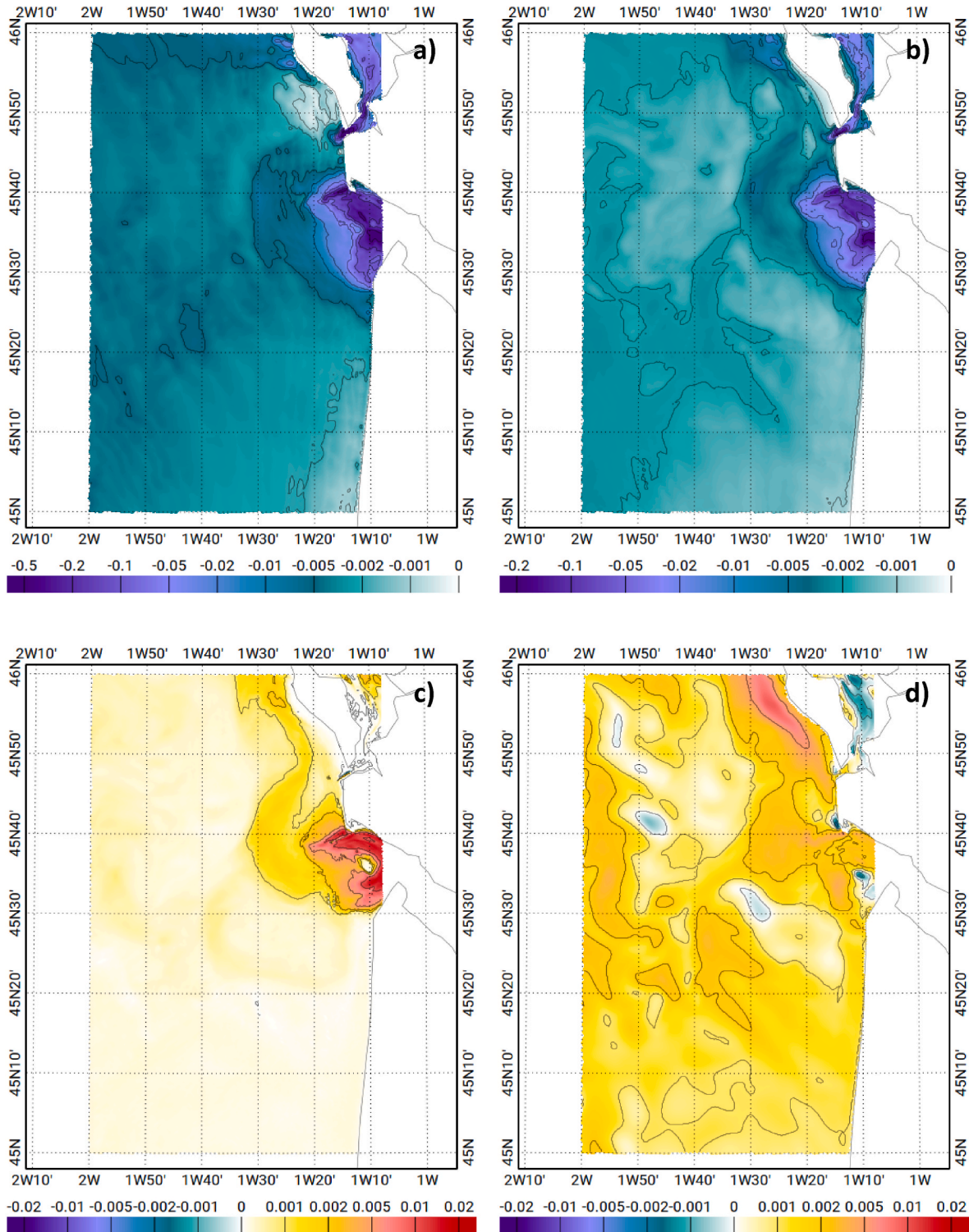


Fig. 18. a) Averaged bottom dissipation, b) internal dissipation, c) buoyancy term and d) wind work (d) ( $W/m^2$ ) between March 9 and March 13, 2011 (bulge period, REF run).

sentative of the amount of energy necessary to break down and mix stratification. Wind work (*WIND*) is an estimation of the wind energy actually transferred to the ocean. Positive values indicate a source (input) of energy in the ocean. Negative values indicate a sink (output) of energy. For these calculations, we use hourly outputs from the REF simulation averaged over a period of 5 days corresponding to the plume configuration of interest.

For the bulge, the energy terms are averaged over the spring to neap transition period (March 9–13 2011, Fig. 18). We can identify two main patterns: for both dissipations and for the buoyancy term, the largest values are obtained at the estuary outlet; bottom dissipation is dominant compared to all the other terms, with absolute values reaching more than 0.5 W/m<sup>2</sup> locally. Bottom dissipation reaches very low values in the northern part of the plume (at 45°N50'). As expected, the spatial distribution of the bottom friction term is highly correlated to the tidal currents (not shown). In the area shown in Fig. 18, the latter are maximum at the estuary mouth and in the narrow pass between the Oléron Island and the continent. At the Cordouan section, M2 tidal currents reach 90 cm/s, while S2 and M4 currents exceed 30 cm/s and 15 cm/s respectively. The currents for the three constituents reach a local minimum west of Oléron Island (1°20'W - 45°50'N).

The buoyancy term highlights the location of the bulge and of the northward coastal current, where the stratification is the strongest on the shelf. Internal dissipation and wind work have globally low values. In the energy terms time series (not shown), an increase of internal dissipation is observed at the end of the bulge period, during the neap to spring transition; it is correlated to the increase of bottom dissipation. This increase is coherent with the destabilization processes described in Section 5.1.2.

In the case of the extended plumes, the levels of energy are much higher than for the bulge case. In particular, the internal dissipation reaches values higher than 0.01 W/m<sup>2</sup> (absolute values) over the whole displayed area in both extended plumes, and up to 0.02 W/m<sup>2</sup> further on the shelf for the NSP (not shown). The buoyancy term reaches values between 0.002 and 0.005 W/m<sup>2</sup> on the shelf for both extended plumes, against 0.001 W/m<sup>2</sup> in the same area during the bulge period. The most striking difference is on the wind work (Fig. 19), with maximum values

above 0.01 W/m<sup>2</sup> in the EP case and up to more than 0.02 W/m<sup>2</sup> in the NSP case, against 0.005 W/m<sup>2</sup> maximum very locally during the bulge period.

For the buoyancy term, the increase between the bulge and the north-south extended plume (NSP) can be mainly attributed to the larger runoff in the case of the NSP (1627 m<sup>3</sup>/s on average with a peak at more than 2000 m<sup>3</sup>/s, against 731 m<sup>3</sup>/s on average for the bulge). For the offshore extended plume, the mean runoff is of the same order as the bulge mean runoff. In this case, the increase in buoyancy is mainly due to the extension of freshwater on the shelf thanks to the relaxation of the bulge occurring before. Upwelling-favorable winds contribute to this transport of freshwater: as detailed in section 5.2.1.

In a general way, the increase in internal dissipation can be explained by either an increase in local wind (with a direct impact on vertical mixing) or by an increase of internal shear due to a change in the circulation. In our case, time series of these terms over the area evidence a strong correlation between the increase in internal dissipation and the increase in local wind work, (not shown). Maximum values of the wind are increased by 46% and 64% for the EP and the NSP respectively, compared to the bulge. At the first order, the shear induced by strong winds is then mostly responsible for the internal dissipation difference between the bulge and the extended plumes. However, in a realistic simulation like this one, it remains difficult to fully disentangle the effect of the wind and of the shelf circulation because the forcings have both direct (instantaneous) and integrated impacts over time.

At the estuary mouth, bottom dissipation is always dominant compared to the other terms. To better estimate this dominance, we calculate the ratio between tidal dissipation and the other terms. We found that bottom dissipation exceeds the internal dissipation by a ratio of 1–5, whatever the type of plume observed (bulge or extended plumes). Compared to the buoyancy term, the ratio is even higher (from 3 to more than 20 within the channel across the Cordouan section). This ratio is more sensitive to the type of plume, with the highest values for the bulge. Finally, bottom dissipation is exceeding wind work by a ratio ranging from 3 to more than 100 in the shallowest areas. This ratio is always the largest in the bulge case.

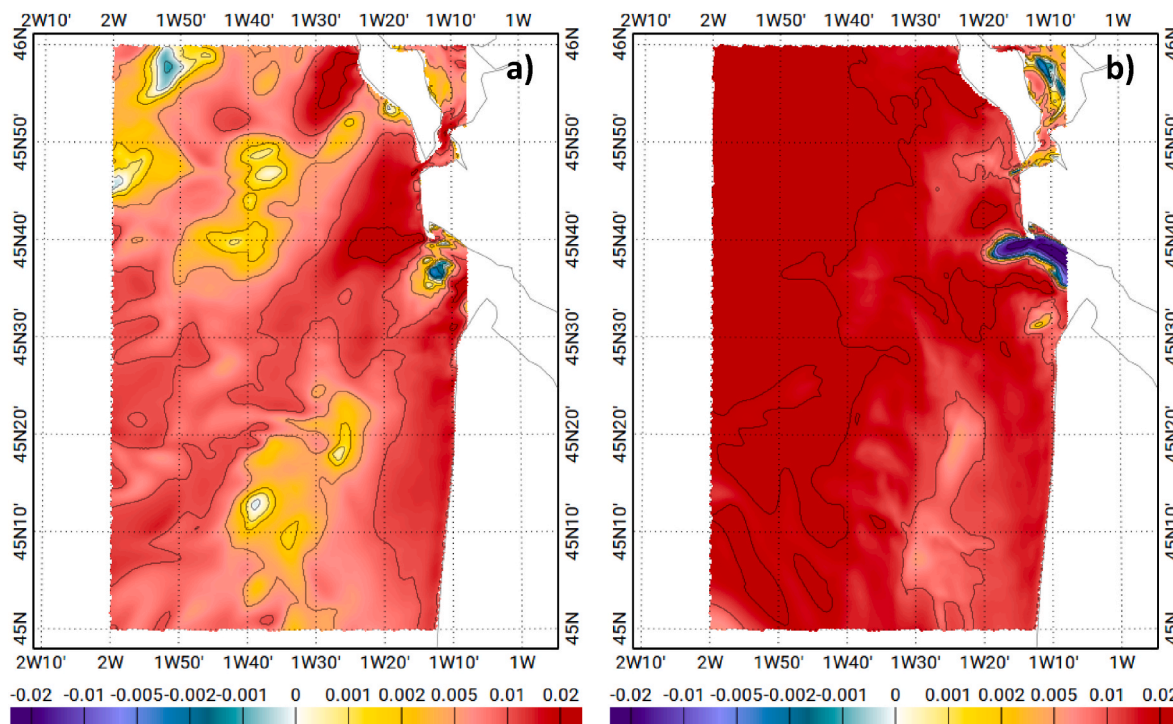


Fig. 19. Wind work (W/m<sup>2</sup>) between a) January 29 and February 2, 2012 (EP) and b) January 3 and January 7, 2012 (NSP).

## 6. Conclusion

In this paper, we analyze the Gironde River plume from a numerical model with a horizontal grid varying in resolution, to resolve both the large scale dynamics in the Bay of Biscay and the smaller scale dynamics of the plume and the river mouth. The objective is to characterize the main pathways of the Gironde waters depending on forcing conditions. We also evidence the impact of tides and wind variability on the plume shape and on its spreading over the shelf using a two-year simulation. The numerical experiments include sensitivity runs to investigate the influence of tides and wind variability on the plume.

The most frequent and well-defined pattern of the plume is an intermittent bulge. The bulge is created in moderate to high discharge conditions and relatively weak wind conditions; its formation is linked to the alternation of spring and neap tides. The latter tends to create the following pattern: (1) formation of a bulge during the transition from spring to neap tides, (2) reinforcement of the bulge in terms of stratification during neap tides, (3) destabilization of the bulge during the neap to spring tides transition, with increased mixing that breaks stratification. When the bulge is relaxed, upwelling favorable winds can export the freshwater offshore; such a situation with a large spreading of the plume over the shelf west and north of the estuary are observed in two cases during our study period. We also evidence two cases with an extended plume northward and southward along the coast: they occur during or just after high discharge events and under strong westerly winds that favor the southward extension of the plume. As the plume expands offshore, low-salinity waters are eventually exported off the shelf.

These results provide a detailed analysis of the plume properties in the near and mid fields and extend previous works that were based either on surface observations or in simpler configurations. Besides, we identify the conditions under which the bulge is formed and destabilized, a useful information to better interpret observations (e.g. ocean turbidity from remote sensing) and to understand other river plumes with similar discharge regimes.

The sensitivity analysis based on the comparison between the different runs shows that the shape of the plume is fundamentally different when tides are neglected and winds filtered. Without tides, the plume flows northward and southward along the coast. In the case with filtered wind, the plume extends further on the shelf in all directions, but as in the reference run there is a much higher probability of occurrence of the plume north of the mouth. The sensitivity runs also reveal that the bulge formation is only possible in the presence of tides and when the wind has a strong enough variability. Our interpretation is that wind-driven mixing on the shelf is essential to ensure a large enough density difference between the shelf waters and the estuarine waters and allow for the bulge dynamics to develop.

The role of tides is not limited to their impact on stratification. Tides also influence the dynamics in the outlet where the circulation is completely different with and without tides. Rectification processes have already been suggested by Mallet et al. (2000), but the novelty here is that we observe the formation of residual vortices in a realistic 3D run and their impact on the circulation and dynamics of the plume. In particular a small anticyclone is systematically present southwest of the Cordouan Island in the periods where a bulge forms; this anticyclone does not exist in the run without tides. Besides, it is strongly weakened in the periods when the river discharge is high, more particularly when it reaches a peak. We suggest this weakening results from the local alteration of tides by the large discharge. Further sensitivity studies would be necessary to disentangle the effect of tidal rectification, of river flow and Ekman currents on the local dynamics over these high discharge periods of several days.

This study evidences the crucial role played by the outlet as a transition area for the estuarine waters: there, tides impact the stratification and constrain the flow through the channel and between small vortices. Therefore, models of the Gironde plume should include in their domain

this transition zone with a fine enough resolution to represent the details of the bottom topography and coastline geometry and thus of the complex residual circulation. We believe that similar conclusions could apply for other estuarine systems.

As a consequence, any factors that could influence tides in this area, such as sea level rise or increased river discharge in the context of global climate change; or human action on the bathymetry, could lead to a significant change in the behavior of the plume.

The approach adopted in this work is complementary to other studies focusing on specific events, such as the one of Ayouche et al. (2021) which documents in a detailed way the instabilities triggered by wind, tides and freshwater inflow during a bulge occurrence. Future work will include longer term simulations of several years to confirm the behavior observed in this study. We also plan to explore the interannual variability of the plume patterns due, in particular, to the interannual changes of the Gironde discharge (e.g. Schmidt, 2020, Jalón-Rojas and Castelle, 2021). Finally, this work is part of the preparation of the SWOT altimetry mission (Fu et al., 2012; Rodriguez et al., 2017), scheduled for launch at the end of 2022. In this context, the observability in satellite altimetry measurements of the signals resulting from the Gironde River plume dynamics will be a main focus of our work. In the future, SWOT data should also help us verify small scale river plume structures obtained by numerical modelling.

## Declaration of competing interest

The authors declare that they have no known competing financial interests or personal relationships that could have appeared to influence the work reported in this paper.

## Acknowledgements

This work is a contribution to the COCTO and COCTO-FO projects (SWOT Science Team Program) funded by CNES. Support from CNES and CNRS/INSU is gratefully acknowledged. This work was performed using HPC resources from GENCI/CINES (grants 2019- A0060110098 and 2020- A0080110098). The authors also thank D. Gazen (Laero) for the use of the Nuwa computing and storage facilities at OMP, Toulouse, France. The SYMPHONIE code is distributed by the French SIROCCO Service (<https://sirocco.obs-mip.fr/>). Many thanks to Puertos del Estado, the SPC Gironde, REFMAR, Météo-France and IFREMER (CORABI database, Islands network), SHOM and OHI for providing the in situ data. The authors gratefully acknowledge the receipt of SSS gridded data from E. Kestenare (LEGOS) and of ASPEX currents data from G. Charria, S. Theetten, L. Marié and A. Le Boyer (IFREMER). Many thanks to F. Lyard (LEGOS) for discussion about tides and for providing us altimetric tidal constituents and to Pierre De Mey-Frémaux for discussions on the manuscript. We also thank T. Duhaut and C. Nguyen for their valuable help with the model grid and SYMPHONIE initial setting. Maps and model-data comparisons for tidal elevations have been partly made using the tools and POCViP software, developed at LEGOS by D. Allain and F. Lyard. This study has been conducted using ECMWF products ([www.ecmwf.int](http://www.ecmwf.int)) and E.U. Copernicus Marine Service Information (product: DATASET-IBI-REANALYSIS-PHYS-005-002-DAILY, produced by Puertos del Estado and Mercator-Ocean, and available at [https://resources.marine.copernicus.eu/?option=com\\_csw&view=details&product\\_id=IBI\\_MULTITYEAR\\_PHY\\_005\\_002](https://resources.marine.copernicus.eu/?option=com_csw&view=details&product_id=IBI_MULTITYEAR_PHY_005_002), last access October 2019). The rivers daily discharges stem from the French Banque Hydro (<http://hydro.eaufrance.fr/>).

## References

- Allen, G.P., Salomon, J.C., Bassoullet, P., Du Penhoat, Y., de Grandpré, C., 1980. Effects of tides on mixing and suspended sediment transport in macrotidal estuaries. *Sediment. Geol.* 26 (1–3), 69–90. [https://doi.org/10.1016/0037-0738\(80\)90006-8](https://doi.org/10.1016/0037-0738(80)90006-8).
- Alory, G., Delcroix, T., Téchiné, P., Diverres, D., Varillon, D., Cravatte, S., Gouriou, Y., Grelet, J., Jacquin, S., Kestenare, E., Maes, C., Morrow, R., Perrier, J., Reverdin, G.,

- Roubaud, F., 2015. The French contribution to the voluntary observing ships network of sea surface salinity. *Deep-Sea Res. Part I Oceanogr. Res. Pap.* 105, 1–18. <https://doi.org/10.1016/j.dsr.2015.08.005>.
- Ayouche, A., Carton, X., Charria, G., Theetten, S., Ayoub, N., 2020. Instabilities and vertical mixing in river plumes: application to the Bay of Biscay. *Geophys. Astrophys. Fluid Dynam.* 114 (4–5), 650–689. <https://doi.org/10.1080/03091929.2020.1814275>.
- Ayouche, A., Charria, G., Carton, X., Ayoub, N., Theetten, S., 2021. Non-linear processes in the Gironde River Plume (North-East Atlantic): instabilities and mixing. *Front. Mar. Sci.* 8, 1–24. <https://doi.org/10.3389/fmars.2021.701773>, 701773.
- Blumberg, A.F., Mellor, G.L., 1987. A description of a three-dimensional coastal ocean circulation model. Three-dimens. *Coast. Ocean Model.* 4, 1–16. <https://doi.org/10.1029/C0004p0001>.
- Byun, D.-S., Hart, D.E., 2020. A monthly tidal envelope classification for semidiurnal regimes in terms of the relative proportions of the S2, N2, and M2 constituents. *Ocean Sci.* 16, 965–977. <https://doi.org/10.5194/os-16-965-2020>.
- Castaing, P., 1984. Rapport I.4 Courantologie de dérive dans les zones côtières à l'aide de bouées positionnées par satellite (système ARGOS). *Journées de l'hydraulique* 18 (1), 1–8.
- Charria, G., Theetten, S., Vandermeirsch, F., Yelekcik, Ö., Audiffren, N., 2017. Interannual evolutions of (sub)mesoscale dynamics in the Bay of Biscay. *Ocean Science Discussions*, January 1–30. <https://doi.org/10.5194/os-2016-92>.
- Chen, Z., Gong, W., Cai, H., Chen, Y., Zhang, H., 2017. Dispersal of the Pearl River plume over continental shelf in summer. *Estuar. Coast Shelf Sci.* 194, 252–262. <https://doi.org/10.1016/j.ecss.2017.06.025>.
- Constantin, S., Doxaran, D., Derkacheva, A., Novoa, S., Lavigne, H., 2018. Multi-temporal dynamics of suspended particulate matter in a macro-tidal river Plume (the Gironde) as observed by satellite data. *Estuar. Coast Shelf Sci.* 202, 172–184. <https://doi.org/10.1016/j.ecss.2018.01.004>.
- Costoya, X., Fernández-Nóvoa, D., deCastro, M., Gómez-Gesteira, M., 2017. Loire and Gironde turbid plumes: characterization and influence on thermohaline properties. *J. Sea Res.* 130 (April), 7–16. <https://doi.org/10.1016/j.seares.2017.04.003>.
- Dukhovskoy, D.S., Morey, S.L., Martin, P.J., O'Brien, J.J., Cooper, C., 2009. Application of a vanishing, quasi-sigma, vertical coordinate for simulation of high-speed, deep currents over the Sigsbee Escarpment in the Gulf of Mexico. *Ocean Model.* 28 (4), 250–265. <https://doi.org/10.1016/j.oceomod.2009.02.009>.
- Ebert, E.E., 2008. Fuzzy verification of high-resolution gridded forecasts: a review and proposed framework. *Meteorol. Appl.* 15 (1), 51–64. <https://doi.org/10.1002/MET.25>.
- Estournel, C., Marsaleix, P., Ulses, C., 2021. A new assessment of the circulation of Atlantic and Intermediate Waters in the Eastern Mediterranean. *Prog. Oceanogr.* 198, 102673. <https://doi.org/10.1016/j.pcean.2021.102673>.
- Etcheber, H., Schmidt, S., Sottolichio, A., Maneux, E., Chabaux, G., Escalier, J.M., Wennekes, H., Derriennic, H., Schmeltz, M., Quémener, L., Repecaud, M., Woerther, P., Castaing, P., 2011. Monitoring water quality in estuarine environments: Lessons from the MAGEST monitoring program in the Gironde fluvial-estuarine system. *Hydro. Earth Syst. Sci.* 15 (3), 831–840. <https://doi.org/10.5194/hess-15-831-2011>.
- Fong, D.A., Geyer, W.R., 2001. Response of a river plume during an upwelling favorable wind event. *J. Geophys. Res.: Oceans* 106 (C1), 1067–1084. <https://doi.org/10.1029/2000JC900134>.
- Froidefond, J.M., Jegou, A.M., Hermida, J., Lazure, P., Castaing, P., 1998. Variabilité du panache turbide de la Gironde par teledetection. Effets des facteurs climatiques. *Oceanol. Acta* 21 (2), 191–207. [https://doi.org/10.1016/S0399-1784\(98\)80008-X](https://doi.org/10.1016/S0399-1784(98)80008-X).
- Fu, L.-L., Alsdorf, D., Morrow, R., Rodriguez, E., Mognard, N., 2012. In: Fu, L.-L. (Ed.), *SWOT: The Surface Water and Ocean Topography Mission: Wide-Swath Altimetric Measurement of Water Elevation on Earth*.
- Gangloff, A., Verney, R., Doxaran, D., Ody, A., Estournel, C., 2017. Investigating Rhône River plume (Gulf of Lions, France) dynamics using metrics analysis from the MERIS 300m ocean color archive (2002–2012). *Continent. Shelf Res.* 144 (June), 98–111. <https://doi.org/10.1016/j.csr.2017.06.024>.
- Garvine, R.W., 1995. A dynamical system for classifying buoyant coastal discharges. *Continent. Shelf Res.* 15 (13), 1585–1596. [https://doi.org/10.1016/0278-4343\(94\)00065-U](https://doi.org/10.1016/0278-4343(94)00065-U).
- Geyer, W.R., MacCready, P., 2014. The estuarine circulation. *Annu. Rev. Fluid Mech.* 46, 175–197. <https://doi.org/10.1146/annurev-fluid-010313-141302>.
- Hansen, D.V., Rattray, M., 1966. New dimensions in estuary classification. *Limnol. Oceanogr.* 11, 319–326.
- Hermida, J., Lazure, P., Froidefond, J.M., Jegou, A.M., Castaing, P., 1998. Seaward dispersion of Gironde estuarine waters on to Aquitanian continental shelf from hydrological, satellite and numeric data. *Oceanol. Acta* 21 (2), 209–221. [https://doi.org/10.1016/S0399-1784\(98\)80009-1](https://doi.org/10.1016/S0399-1784(98)80009-1).
- Hetland, R.D., Hsu, T.J., 2013. Freshwater and sediment dispersal in large river plumes. In: *Biogeochemical Dynamics at Major River-Coastal Interfaces*, pp. 55–85. <https://doi.org/10.1017/cbo9781139136853.006>.
- Horner-Devine, A.R., Hetland, R.D., MacDonald, D.G., 2015. Mixing and transport in coastal river plumes. *Annu. Rev. Fluid Mech.* 47, 569–594. <https://doi.org/10.1146/annurev-fluid-010313-141408>.
- Isobe, A., 2005. Ballooning of river-plume bulge and its stabilization by tidal currents. *J. Phys. Oceanogr.* 35 (12), 2337–2351. <https://doi.org/10.1175/JPO2837.1>.
- Jalón-Rojas, I., Castelle, B., 2021. Climate control of multidecadal variability in River Discharge and precipitation in Western Europe. *Water* 13, 257. <https://doi.org/10.3390/w13030257>.
- Kersalé, M., Marié, L., Le Cann, B., Serpette, A., Lathuilière, C., Le Boyer, A., Rubio, A., Lazure, P., 2016. Poleward along-shore current pulses on the inner shelf of the Bay of Biscay. *Estuar. Coast Shelf Sci.* 179, 155–171. <https://doi.org/10.1016/j.ecss.2015.11.018>.
- Kourafalou, V.H., 1999. Process studies on the Po River plume, North Adriatic Sea. *Journal of Geophysical Research-Oceans* 104 (C12), 29963–29985. <https://doi.org/10.1029/1999jc900217>.
- Lazure, P., Jégou, A.M., 1998. 3D modelling of seasonal evolution of Loire and Gironde plumes on Biscay Bay continental shelf. *Oceanol. Acta* 21 (2), 165–177. [https://doi.org/10.1016/S0399-1784\(98\)80006-6](https://doi.org/10.1016/S0399-1784(98)80006-6).
- Le Boyer, A., Charria, G., Le Cann, B., Lazure, P., Marié, L., 2013. Circulation on the shelf and the upper slope of the Bay of Biscay. *Continent. Shelf Res.* 55, 97–107. <https://doi.org/10.1016/j.csr.2013.01.006>.
- Li, M., Rong, Z., 2012. Effects of tides on freshwater and volume transports in the Changjiang River plume. *J. Geophys. Res.: Oceans* 117 (6), 1–15. <https://doi.org/10.1029/2011JC007716>.
- Liu, Y., MacCready, P., Hickey, B.M., Dever, E.P., Kosro, P.M., Banas, N.S., 2009. Evaluation of a coastal ocean circulation model for the Columbia River plume in summer 2004. *J. Geophys. Res.* 114, 1–23. <https://doi.org/10.1029/2008JC004929>.
- Lyard, F.H., Allain, D.J., Cancet, M., Carrère, L., Picot, N., 2021. FES2014 global ocean tide atlas: design and performance. *Ocean Sci.* 17 (3), 615–649. <https://doi.org/10.5194/os-17-615-2021>.
- MacCready, P., Banas, N.S., Hickey, B.M., Dever, E.P., Liu, Y., 2009. A model study of tide- and wind-induced mixing in the Columbia River Estuary and plume. *Continent. Shelf Res.* 29 (1), 278–291. <https://doi.org/10.1016/j.csr.2008.03.015>.
- Mallet, C., Howa, H., Garlan, T., Sottolichio, A., Le Hir, P., Michel, D., 2000. Utilisation of numerical and statistical techniques to describe sedimentary circulation patterns in the mouth of the Gironde estuary. In: *Comptes Rendus de l'Académie de Sciences - Serie Ila: Sciences de La Terre et Des Planetes*, vol. 331, pp. 491–497. [https://doi.org/10.1016/S1251-8050\(00\)01437-3](https://doi.org/10.1016/S1251-8050(00)01437-3), 7.
- Marsaleix, P., Auclair, F., Estournel, C., 2006. Considerations on open boundary conditions for regional and coastal ocean models. *J. Atmos. Ocean. Technol.* 23, 1604–1613. <https://doi.org/10.1175/JTECH1930.1>.
- Marsaleix, P., Auclair, F., Floor, J.W., Herrmann, M.J., Estournel, C., Piraud, I., Ulses, C., 2008. Energy conservation issues in sigma-coordinate free-surface ocean models. *Ocean Model.* 20 (1), 61–89. <https://doi.org/10.1016/j.oceomod.2007.07.005>.
- Michaud, H., Marsaleix, P., Leredde, Y., Estournel, C., Bourrin, F., Lyard, F., Mayet, C., Arduini, F., 2012. Three-dimensional modelling of wave-induced current from the surf zone to the inner shelf. *Ocean Sci.* 8 (4), 657–681. <https://doi.org/10.5194/os-8-657-2012>.
- Nash, J.D., Kilcher, L.F., Moum, J.N., 2009. Structure and composition of a strongly stratified, tidally pulsed river plume. *J. Geophys. Res.: Oceans* 114 (8), 1–16. <https://doi.org/10.1029/2008JC005036>.
- Nguyen-Duy, T., Ayoub, N.K., Marsaleix, P., Toulblanc, F., De Mey-Frémaux, P., Piton, V., Herrmann, M., Duhaut, T., Tran, M.C., Ngo-Duc, T., 2021. Variability of the Red River plume in the Gulf of Tonkin as revealed by numerical modeling and clustering analysis. *Front. Mar. Sci.* <https://doi.org/10.3389/fmars.2021.772139>.
- Petus, C., Marieu, V., Novoa, S., Chust, G., Bruneau, N., Froidefond, J.M., 2014. Monitoring spatio-temporal variability of the Adour River turbid plume (Bay of Biscay, France) with MODIS 250-m imagery. *Continent. Shelf Res.* 74, 35–49. <https://doi.org/10.1016/j.csr.2013.11.011>.
- Piton, V., Herrmann, M., Marsaleix, P., Duhaut, T., Ngoc, T.B., Tran, M.C., Shearman, K., Ouilon, S., 2021. Influence of winds, geostrophy and typhoons on the seasonal variability of the circulation in the Gulf of Tonkin: a high-resolution 3D regional modeling study. *Regional Studies in Marine Science* 45, 101849. <https://doi.org/10.1016/j.rsma.2021.101849>.
- Puillat, I., Lazure, P., Jégou, A.M., Lampert, L., Miller, P.L., 2004. Hydrographical variability on the French continental shelf in the Bay of Biscay, during the 1990s. *Continent. Shelf Res.* 24 (10), 1143–1163. <https://doi.org/10.1016/j.csr.2004.02.008>.
- Reverdin, G., Kestenare, E., Frankignoul, C., Delcroix, T., 2007. Surface salinity in the Atlantic Ocean (30°S–50°N). *Prog. Oceanogr.* 73 (3–4), 311–340. <https://doi.org/10.1016/j.pcean.2006.11.004>.
- Reverdin, G., Marié, L., Lazure, P., D'Ovidio, F., Boutin, J., Testor, P., Martin, N., Lourenco, A., Gaillard, F., Lavin, A., Rodriguez, C., Somavilla, R., Mader, J., Rubio, A., Blouch, P., Rolland, J., Bozec, Y., Charria, G., Batifoulier, F., et al., 2013. Freshwater from the Bay of Biscay shelves in 2009. *J. Mar. Syst.* 109, S134–S143.
- Rodriguez, E., Fernandez, D.E., Peral, E., Chen, C.W., Bleser, J. De, Williams, B., 2017. Wide-swath altimetry: a review. In: *Satellite Altimetry over Oceans and Land Surfaces*. Taylor and Francis (in press).
- Rong, Z., Li, M., 2012. Tidal effects on the bulge region of Changjiang River plume. *Estuar. Coast Shelf Sci.* 97, 149–160. <https://doi.org/10.1016/j.ecss.2011.11.035>.
- Ross, L., Huguénard, K., Sottolichio, A., 2019. Intra-tidal and fortnightly variability of vertical mixing in a macrotidal estuary: the Gironde. *J. Geophys. Res.: Oceans* 124 (4), 2641–2659. <https://doi.org/10.1029/2018JC014456>.
- Ruault, V., Jouanno, J., Durand, F., Chanut, J., Benshila, R., 2020. Role of the tide on the structure of the Amazon plume: a Numerical modeling approach. *J. Geophys. Res.: Oceans* 125 (2), 1–17. <https://doi.org/10.1029/2019jc015495>.
- Schmidt, S., 2020. A 14-Year Multi-Sites and High-Frequency Monitoring of Salinity in the Tidal Garonne River (S-W France) Reveals Marked Inter-annual Variability in Marine Intrusion, pp. 3–11. [https://doi.org/10.1007/978-981-15-2081-5\\_1](https://doi.org/10.1007/978-981-15-2081-5_1).
- Siddorn, J.R., Furner, R., 2013. An analytical stretching function that combines the best attributes of geopotential and terrain-following vertical coordinates. *Ocean Model.* 66, 1–13. <https://doi.org/10.1016/j.oceomod.2013.02.001>.
- Sottolichio, A., Hir, P., Le, Castaing, P., 2001. Modeling mechanisms for the stability of the turbidity maximum in the Gironde estuary, France. *Proc. Mar. Sci.* 3 (C), 373–3.

- Szekely, T., Bezaud, M., Pouliquen, S., Reverdin, G., Charria, G., 2017. CORA-IBI, Coriolis Ocean Dataset for Reanalysis for the Ireland-Biscay-Iberia Region. SEANOE. <https://doi.org/10.17882/50360>.
- Tarya, A., Van der Vegt, M., Hoitink, A.J.F., 2015. Wind forcing controls on river plume spreading on a tropical continental shelf. *J. Geophys. Res.: Oceans* 120 (1), 16–35. <https://doi.org/10.1002/2014JC010456>.
- Toublanc, F., Ayoub, N.K., Lyard, F., Marsaleix, P., Allain, D.J., 2018. Tidal downscaling from the open ocean to the coast: a new approach applied to the Bay of Biscay. *Ocean Model.* 124 <https://doi.org/10.1016/j.ocemod.2018.02.001>.
- Valle-Levinson, A., 2010. *Contemporary Issues in Estuarine Physics*. Cambridge University Press.
- Wang, Y., Xue, H., Chai, F., Chao, Y., Farrara, J., 2014. A model study of the copper River plume and its effects on the northern Gulf of Alaska topical collection on the 5th International workshop on modelling the ocean (IWMO) in Bergen, Norway 17-20 June 2013. *Ocean Dynam.* 64 (2), 241–258. <https://doi.org/10.1007/s10236-013-0684-3>.
- Yankovsky, A.E., Chapman, D.C., 1997. A simple theory for the fate of buoyant coastal discharges. *J. Phys. Oceanogr.* 27 (7), 1386–1401. <https://doi.org/10.1175/1520-0485>.
- Yu, X., Guo, X., Gao, H., 2020. Detachment of low-salinity Water from the Yellow River Plume in summer. *J. Geophys. Res.: Oceans* 125 (10), 1–19. <https://doi.org/10.1029/2020JC016344>.
- Zu, T., Wang, D., Gan, J., Guan, W., 2014. On the role of wind and tide in generating variability of Pearl River plume during summer in a coupled wide estuary and shelf system. *J. Mar. Syst.* 136 (1), 65–79. <https://doi.org/10.1016/j.jmarsys.2014.03.005>.